ENVIRONMENTAL RESEARCH
LETTERS

OPEN ACCESS

RECEIVED
24 August 2020

REVISED
14 July 2021

ACCEPTED FOR PUBLICATION
3 August 2021

PUBLISHED
7 September 2021

LETTER

Moisture and temperature influences on nonlinear vegetation trends in Serengeti National Park

Ningyuan Huang[1,2], **Pinki Mondal**[3,4], **Benjamin I Cook**[5,6] **and Sonali McDermid**[5,7,*]

[1] Department of Applied Mathematics & Statistics, Johns Hopkins University, Baltimore, MD, United States of America
[2] Mathematical Institute for Data Science, Johns Hopkins University, Baltimore, MD, United States of America
[3] Department of Geography and Spatial Sciences, University of Delaware, Newark, DE, United States of America
[4] Department of Plant and Soil Sciences, University of Delaware, Newark, DE, United States of America
[5] NASA Goddard Institute for Space Studies, New York, NY, United States of America
[6] Lamont-Doherty Earth Observator, Columbia University, Palisade, NY, United States of America
[7] Department of Environmental Studies, New York University, New York, NY, United States of America
[*] Author to whom any correspondence should be addressed.

E-mail: sps246@nyu.edu

Keywords: vegetation, protected areas, climate change, EEMD

Abstract

While long-term vegetation greening trends have appeared across large land areas over the late 20th century, uncertainty remains in identifying and attributing finer-scale vegetation changes and trends, particularly across protected areas. Serengeti National Park (SNP) is a critical East African protected area, where seasonal vegetation cycles support vast populations of grazing herbivores and a host of ecosystem dynamics. Previous work has shown how non-climate drivers (e.g. land use) shape the SNP ecosystem, but it is still unclear to what extent changing climate conditions influence SNP vegetation, particularly at finer spatial and temporal scales. We fill this research gap by evaluating long-term (1982–2016) changes in SNP leaf area index (LAI) in relation to both temperature and moisture availability using Ensemble Empirical Mode Decomposition and Principal Component Analysis with regression techniques. We find that SNP LAI trends are nonlinear, display high sub-seasonal variation, and are influenced by lagged changes in both moisture and temperature variables and their interactions. LAI during the long rains (e.g. March) exhibits a greening-to-browning trend reversal starting in the early 2000s, partly due to antecedent precipitation declines. In contrast, LAI during the short rains (e.g. November, December) displays browning-to-greening alongside increasing moisture availability. Rising temperature trends also have important, secondary interactions with moisture variables to shape these SNP vegetation trends. Our findings show complex vegetation-climate interactions occurring at important temporal and spatial scales of the SNP, and our rigorous statistical approaches detect these complex climate-vegetation trends and interactions, while guarding against spurious vegetation signals.

1. Introduction

Recently, a great deal of work has been carried out to identify and attribute late 20th century vegetation changes, namely an inter-annual 'greening' trend at global and regional spatial scales. While the full extent and causes of these trends are still under investigation (Cortés *et al* 2021, Walker *et al* 2020), CO_2-fertilization, land cover change, and agricultural intensification may be important regional drivers (Forkel *et al* 2016, Zhu *et al* 2016, Chen *et al* 2019, Walker *et al* 2020). At smaller spatial scales, however, particularly across global protected areas such as IUCN Wilderness and National Parks (Stolton *et al* 2013), challenges remain in detecting and attributing vegetation changes and their drivers (Mondal *et al* 2020). Protected areas provide critical ecosystem services and sources of human livelihood, and quantifying their vegetation changes, particularly in response to anthropogenic forcings, are important for biodiversity goals.

Prior work has identified increasing land use as one major driver of ecosystem change in protected areas (Venter *et al* 2016, Jones *et al* 2018), particularly

across Africa. In East Africa, land use change is critical to explain recent ecosystem shifts, e.g. to woodier vegetation in savannas, and vegetation productivity declines across protected areas (Landmann and Dubovyk 2014, Midgley and Bond 2015, Probert *et al* 2019, Kija *et al* 2020). Yet, additional work is also needed to identify how climate change may contribute to vegetation trends in East African protected areas (Midgley and Bond 2015, Adole *et al* 2018). These ecosystems' responses to intensifying climate change are uncertain due in part to an incomplete understanding of climate-vegetation interactions, difficulty in detecting robust climate change signals (e.g. precipitation trends), differences in the scales and appropriateness of ecosystem indicators, and limitations on widespread, frequent ground observations (Pettorelli *et al* 2012, Rannow *et al* 2014, Mondal *et al* 2020).

However, advances in satellite and other remote-sensing measures are enabling improved quantification of historical vegetation change and variability across Africa (Pettorelli *et al* 2012, Adole *et al* 2016, Hawinkel *et al* 2016). These products have been used to evaluate vegetation sensitivities at large spatial scales and identify complex vegetation-climate interactions. While many African ecosystems are water-limited (Nemani *et al* 2003, Zhang *et al* 2006, Ugbaje and Bishop 2020), recent studies have explored vegetation dependencies on other environment and climate variables and interactions between them (Ryan *et al* 2017, Adole *et al* 2018). For example, precipitation responses of African vegetation, even in water-limited ecosystems, may be strongly mediated through interactions with thermal plant-growth thresholds and temperature effects (Adole *et al* 2016, 2019), which warrant further investigation under changing climate conditions.

While these water-temperature interactions are generally important across Africa, in East Africa, precipitation variability remains a key driver of vegetation change (Nicholson *et al* 2017, Wei *et al* 2018). The El Niño-southern oscillation (ENSO) and Indian Ocean surface temperatures drive precipitation variability that explains much of the historic normalized difference vegetation index (NDVI) variability in East Africa (Hawinkel *et al* 2016). Additionally, during the late 20th century, intra-annual vegetation variability may have increased across East Africa (Ritchie *et al* 2008), particularly in protected areas in response to precipitation trends (Pettorelli *et al* 2012). A recent study controlling for land use change shows that East African woodland and savannas areas exhibit a delayed start to the growing season, thereby contributing to enhanced seasonal vegetation variability (Adole *et al* 2018). Embedded in this increasing variability may be long-term vegetation trends and even nonlinear responses to changing climate variables, in which temporal trends display 'reversals' (e.g. from greening to browning) (Pettorelli *et al* 2012, Wei *et al* 2018, Kalisa *et al* 2019).

Furthermore, seasonal timescales, the short rains (November–December) and long rains (March–May), are also important when evaluating East African vegetation responses to climate change, particularly precipitation. Nicholson *et al* (2017) highlighted key differences in East African atmospheric circulation between these seasons, which are subject to different modes of externally-forced variability (e.g. pronounced ENSO impacts on short rains) with distinct responses to climate change. Even within the long rains, March, April, and May exhibit substantial differences in the governing modes of rainfall variability, relatively low spatial coherence, and weak correlations in precipitation across the three months (Camberlin and Philippon 2002, Camberlin and Okoola 2003, Camberlin *et al* 2009, Nicholson 2015, Nicholson *et al* 2017). Thus, vegetation responses may also be distinct on monthly timescales.

We herein investigate vegetation changes within Serengeti National Park (SNP), a highly-protected ecosystem where land use activities are relatively restricted per IUCN Category II (Stolton *et al* 2013, Kija *et al* 2020), allowing us to better identify potential climate-driven trends. The SNP supports one of the world's 'great migrations' of herbivores following seasonal vegetation availability (Sinclair *et al* 2008). Increasing climate change and variability, in addition to other anthropogenic pressures, may disrupt key ecosystem processes related to vegetation growth and phenology, with subsequent impacts on both wildlife and human populations (Ritchie *et al* 2008, Sinclair *et al* 2014, Byrom *et al* 2015, Dublin and Ogutu 2015, Kilungu *et al* 2017, Hunninck *et al* 2020). There is uncertainty, however, regarding the presence and timing of SNP vegetation trends. Some studies indicate annual NDVI declines since 1982 across the Serengeti-Mara ecosystem (Pettorelli *et al* 2012, Kalisa *et al* 2019), while others suggest nonlinear trends, with annual browning since the early 2000 s (Wei *et al* 2018). In addition, intra-annual variability of SNP-averaged net primary production may be increasing (Pettorelli *et al* 2012), possibly as a result of increased rainfall variability across the greater Serengeti-Mara ecosystem surrounding the SNP (Ogutu *et al* 2008, Bartzke *et al* 2018). These site-based studies also show increased dry season rainfall alongside annual rainfall declines since the early 2000s, possibly a response to rising Indian Ocean sea surface temperatures (Williams and Funk 2011). Notably, grazing pressure at the edges of the Serengei-Mara ecosystem may indirectly reduce maximum leaf area within the park boundaries, potentially changing vegetation-precipitation interactions (Estes *et al* 2012, Probert *et al* 2019, Veldhuis *et al* 2019, Kija *et al* 2020). We therefore acknowledge that the SNP ecosystem is not fully isolated from land use effects.

Nevertheless, there remain outstanding research gaps to characterize long-term vegetation trends across the SNP at seasonal and monthly scales, and to identify how changing, interactive climate variables contribute to these trends (Adole *et al* 2016). Identifying these vegetation trends requires rigorous statistical methods, for prior work using simplified techniques (Chen *et al* 2019) has likely overestimated the prevalence of global greening (Cortés *et al* 2021). It is also unclear if there are nonlinear vegetation responses (i.e. trend reversals) in the SNP, similar to those appearing across greater East Africa. Here, we fill these research gaps with a novel investigation of spatially-explicit, time-varying, and sub-seasonal SNP vegetation trends in response to changing precipitation, soil moisture, and temperature. Our methods provide a robust, rigorous approach to evaluate vegetation trends, and account for the lagged interactions between moisture and temperature variables in their contributions to these trends. More specifically, we apply ensemble empirical mode decomposition (EEMD) along with principal component analysis (PCA) and regression techniques to a widely-used satellite-derived leaf area index (LAI) product to answer the following research questions: (1) what types of vegetation trends (monotonic greening/browning or nonlinear) are occurring at annual, seasonal, and monthly scales across the SNP? and (2) how do climate variables and their interactions contribute to these SNP LAI trends?

2. Methods

2.1. Study area: SNP

The SNP is situated on the border of Kenya and Tanzania (figure 1), covering 14 763 km^2 at altitudes of 1000–1800 m (Sinclair *et al* 2008). A west-to-east precipitation gradient partly shapes transitions in vegetation classes between acacia-dominated woodlands in the west and south, grasslands to the southeast, and grass and shrublands in the east and north (figure 1). Consequently, LAI (figure A1(a)), the ratio of green leaf area to unit ground area (m^2/m^2), ranges from 0.75 for grass and shrubland regions to 2.5 in savanna areas with a mix of grass and trees. Figure A1 also displays annual average (2003–2016) spatial patterns of soil moisture, precipitation, and surface temperature to further contextualize regional LAI.

The SNP's annual precipitation cycle is characterized by the shifting Intertropical Convergence Zone, which results in two general rainy seasons (Sinclair *et al* 2008): the short rains (November–December) and the long rains (March–May) (figure 2(c)). Climatic influences on precipitation can also be distinct on monthly timescales (Nicholson *et al* 2017), however, and thus we evaluate SNP vegetation and climate trends for each month. The seasonal soil moisture cycle (figure 2(b)) is consistent with rainfall, with a slight decrease in January–February and a peak around April. Regional SNP LAI increases at the beginning of short rains and stays relatively high until May, at which point it declines into the dry season (figure 2(a)), although we note there is much interannual variability in the timing and spatial distribution of green-up and maximum SNP LAI (figure C3).

2.2. Data

We evaluate vegetation change in the SNP using satellite-derived estimates of LAI, as it provides a more direct physiological interpretation of vegetation growth than the NDVI, which is a proxy for greenness (Cook and Pau 2013). LAI is positively and mostly linearly related to net primary productivity (NPP) (Goward and N 1985, Li *et al* 2017), although this linearity diminishes for dense canopies. We use monthly mean LAI from the global LAI3g product (Zhu *et al* 2013) (table 1), which spans July 1981 to December 2016 and is derived from the third generation GIMMS NDVI3g data set at 1/12 degree resolution, 15-day composites. A set of neural networks is used to predict LAI from NDVI, supervised by an improved version of Terra Moderate Resolution Imaging Spectroradiometer LAI (MODIS BNU, Yuan *et al* (2011)) for the overlapping period 2000–2009 period. The trained neural networks are then used to infer LAI for the remaining years. LAI3g compares well with ground LAI measurements and other satellite-based estimates (Zhu *et al* 2013) and has been used widely in many previous ecosystem studies (Cook and Pau 2013, Zhu *et al* 2016, Chen *et al* 2019). We also conduct spatial and temporal correlation analyses using the MODIS LAI as a 'benchmark' to assess the suitability of LAI3g for this study and its similarity to other LAI products (table 1).

2.3. Evaluating time-varying changes to seasonal LAI

To identify the magnitude and direction of any intrinsic vegetation trend, we seek to remove the periodic components, e.g. due to climate variability such as ENSO, from the overall LAI signal. Moreover, we do not limit our trend identification to linear trends only, as nonlinear trends may capture important vegetation-climate interactions. Thus, we decompose the underlying vegetation trend using an established method: EEMD (Wu and Huang 2009). EEMD has been employed in previous studies to identify key modes of vegetation variability, including in East Africa, particularly in relation to precipitation variability (e.g. Hawinkel *et al* 2016, Zhu *et al* 2016, Wei *et al* 2018). EEMD has been shown to be more effective in trend identification than Mann–Kendall tests, especially if the trend magnitude is small compared to other components of the signal (Sang *et al* 2014). Its core algorithm, empirical mode decomposition (EMD) (Huang *et al* 1998), decomposes the LAI time

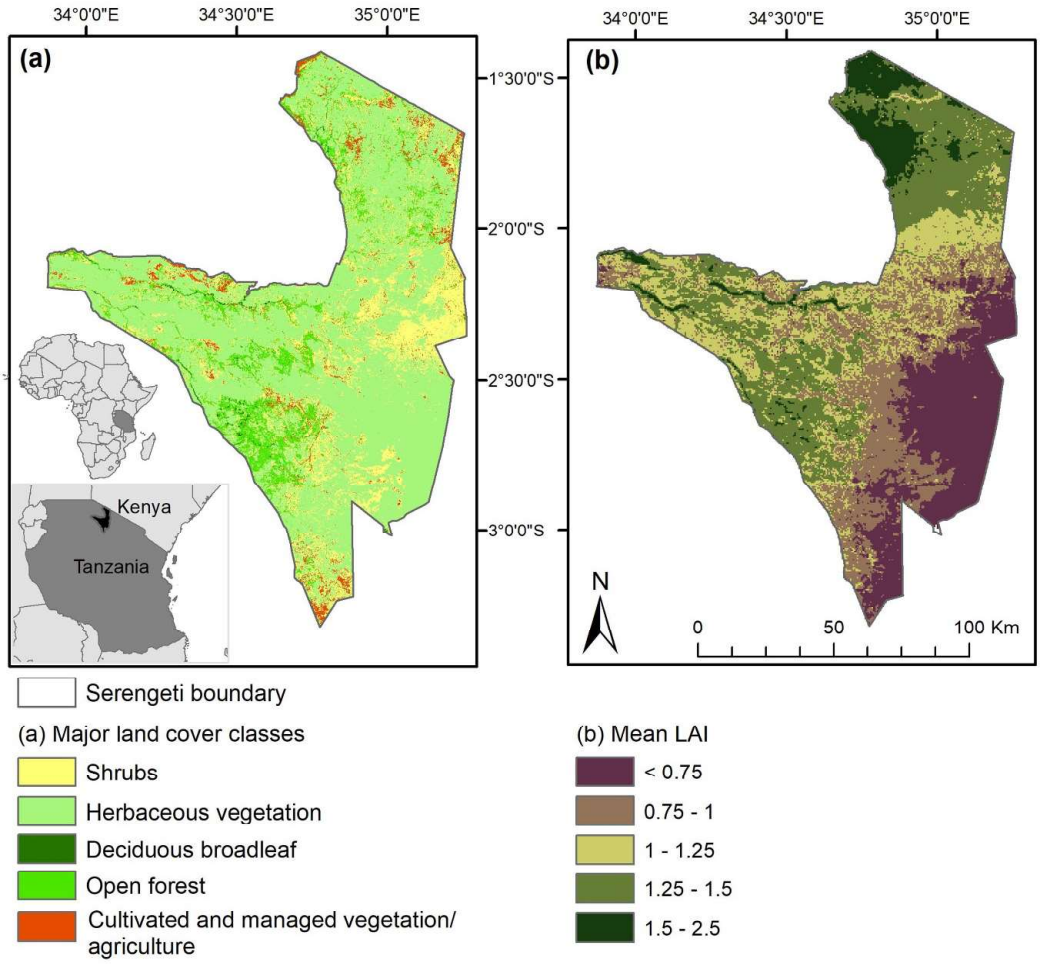

Figure 1. (a) Study area location and major vegetation classes. SNP shapefile obtained from the World Database of Protected Areas; land cover classifications obtained from Copernicus Global Land Cover Layers: CGLS-LC100 collection 2. (b) Annual mean LAI from the global LAI3g product (see table 1 for more details).

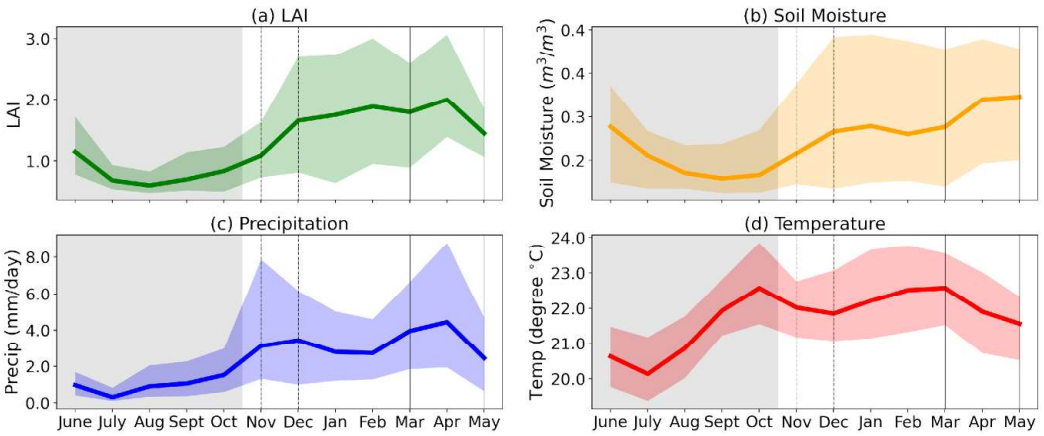

Figure 2. 1982–2016 monthly averages over the SNP for (a) LAI in green (solid line), (b) GLEAM soil moisture in orange (dotted line), (c) CHIRPS precipitation in blue (dashed line), and (d) CRU TS surface temperature in red (dashed-dotted line). Grey (white) background color within the plot corresponds to dry (wet) season. Vertical dashed (solid) lines indicate the short-rain (long-rain) months. Shaded envelopes represent the monthly maximum and minimum for each variable.

Table 1. Brief description of LAI products and its related climate variables products.

Category	Data product short name	Spatial coverage and resolution	Temporal coverage used	Reference
LAI	MODIS LAI	Global, 500 m	4-day averaged to monthly; 4 July 2002 to present	Myneni *et al* (2015)
LAI	LAI3g	Global, 1/12 degree	Semi-monthly averaged to monthly; July 1981 to December 2016	Zhu *et al* (2013)
LAI	GLASS	Global, 0.05 degree	8-day averaged to monthly; 1981–2017	Liang *et al* (2013)
LAI	CDR	Global, 0.05 degree	Daily averaged to monthly; 24 June 1981 to present	Claverie *et al* (2016)
Precipitation	CHIRPS	Global, 0.05 degree	Daily averaged to monthly; 1981 to present	Funk *et al* (2015)
Soil moisture	GLEAM v.3	Global, 0.25 degree	Monthly; 1980–2018. root soil moisture.	Martens *et al* (2017)
Temperature	CRU TS v.4	Global, 0.5 degree	Monthly; 1901–2019	Harris *et al* (2020)

series into a finite number of oscillatory, intrinsic mode functions (IMFs), and a smooth residual term:

$$LAI(t) = \sum_i IMF_i(t) + Trend(t). \quad (1)$$

We hereafter use 'Trend' to refer to the decomposed Trend component from our EEMD specifically (figure 3(a)). To obtain a more robust decomposition, EEMD ensembles multiple trials of EMD, each of which decomposes the original time series perturbed with white noise. We perform EEMD on SNP LAI for each month at each pixel (196 grid cells, 35 years) using 100 trials with a noise amplitude 0.05 of the absolute signal amplitude. We decompose at most three IMF modes and, similar to Wei *et al* (2018), categorize the remaining Trend into: strictly greening or strictly browning (i.e. monotonic Trend); greening-to-browning or browning-to-greening (i.e. nonlinear or inflected Trend); and undetermined (i.e. more than one extrema). To determine if strictly greening or browning montonic Trends are significant, we assess whether they are statistically different from random noise that preserves the original LAI distribution and autocorrelation structures (i.e. surrogates), measured by a test statistic. We use iteratively refined amplitude adjusted Fourier transform method (IAAFT, appendix B) (Schreiber and Schmitz 1996) to generate these surrogates for monthly LAI series. We choose the time reversibility (TR) as our test statistic:

$$TR = \frac{1}{n}\sum_{t=1}^{n-1}(X_t X_{t+1}^2 - X_t^2 X_{t+1}) \quad (2)$$

where X_t is the value at time t, and n is the number of time steps. If a significant monotonic Trend is present, the TR magnitude will be large since reversing the data in time will differ substantially from the original trend. We performed a one-sided test at the 5% significance level by generating 19 surrogates from the original monthly LAI and extracting their Trends with EEMD. The LAI Trend is significant when its TR statistic magnitude is greater than the TR statistics from all the other surrogates' trends. By testing on the LAI Trend alone, this procedure avoids false positive trends found in other studies of global greening (Cortés *et al* 2021), which may result from longer-term modes of ecosystem variability. Details on the surrogate generation and significance test can be found in appendix B.

Nonlinear Trends may constitute another interesting response in which the LAI Trend has 'reversed' over time. Such trend reversals have been documented in other vegetation studies (de Jong *et al* 2013, Pan *et al* 2018, Wei *et al* 2018), and could result from changing, interactive external forcing conditions and nonlinear vegetation responses.

Lastly, we evaluate how the Trend contributes to the overall LAI signal, i.e. how much of the total LAI variance the Trend explains, using the variance contribution rate (VCR), a standard metric used with EEMD approaches in previous climate studies (e.g. Bai *et al* 2015, Guo *et al* 2016, Liu *et al* 2020):

$$VCR_{Trend} = \frac{\sigma^2_{Trend}}{\sum_i \sigma^2_{IMF_i} + \sigma^2_{Trend}} \quad (3)$$

where σ^2 represents the variance for the IMF or the trend component.

2.4. Evaluating the contribution of changing climate variables to SNP LAI change

We further investigate the contributions to the SNP LAI Trends by key regional climate variables (figure 2, table 1): root zone soil moisture from the global land evaporation Amsterdam model (GLEAM) (Martens *et al* 2017); precipitation from the climate hazards group infrared precipitation with stations (CHIRPS) (Funk *et al* 2015); and surface temperature from CRU Surface Temperature Version 4 (CRU TS) (Harris *et al* 2020).

We first conduct the above EEMD analysis on each of the climate variables (figure 3(a)). Due to the higher variability present in precipitation and soil moisture, we use a maximum of four IMF modes for

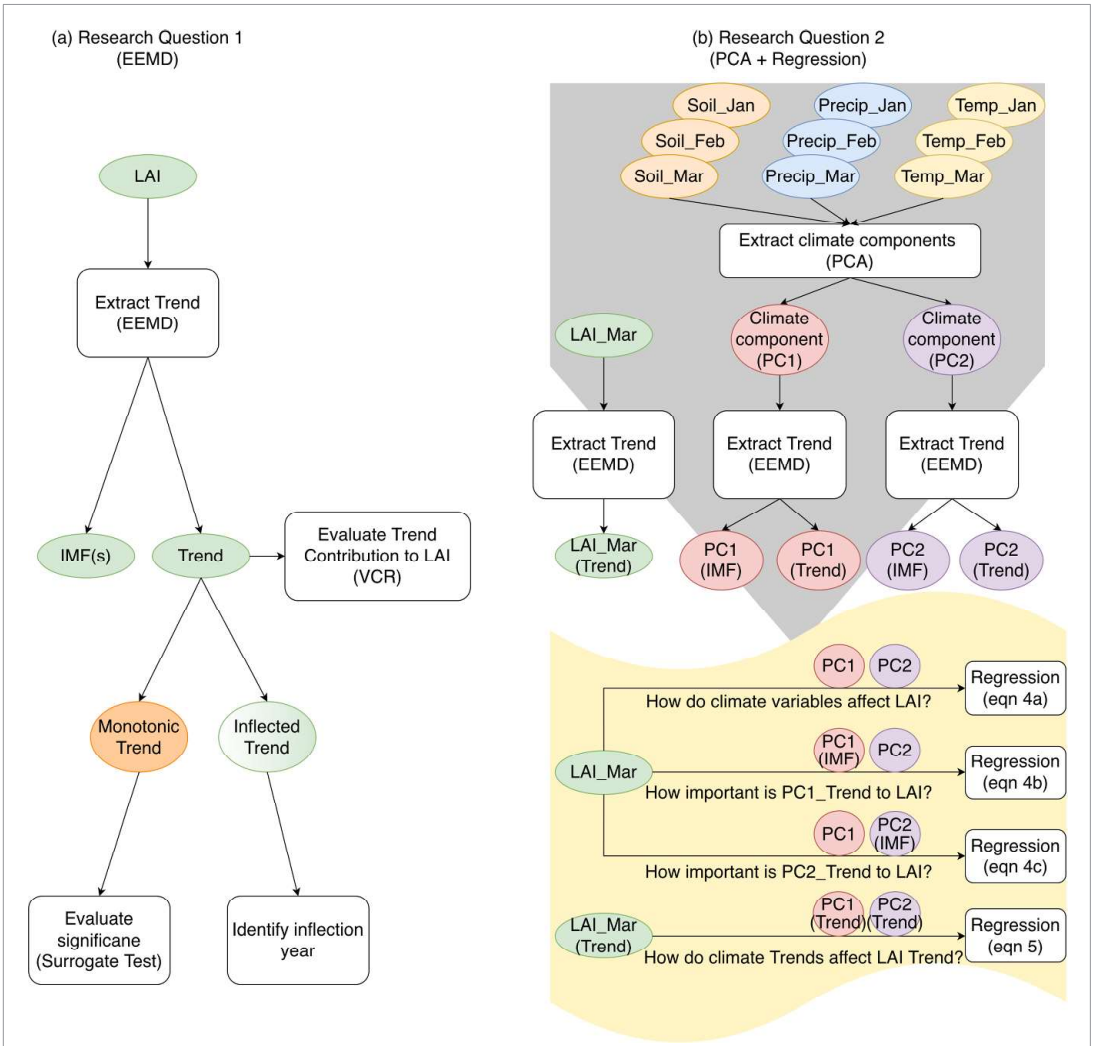

Figure 3. Flow diagrams on (a) evaluating LAI trend using EEMD to answer research question 1; (b) evaluating contributions of climate variables to LAI using PCA and regression techniques to answer research question 2.

all the climate variables. We then perform the same Trend categorization to identify systematic patterns that may relate to the LAI Trends.

Next, we identify months with spatially-uniform Trends (e.g. domain-wide browning) from EEMD analysis. For these month(s), we then take the SNP area-average for the time-varying (1982–2016) climate variables and LAI, with intention of regressing the LAI timeseries on those of the climate variables. However, multicollinearities likely exist between soil moisture, precipitation, and temperature, and their lags, which complicate interpreting their effects as independent variables in a regression. To mitigate these effects, we first apply a PCA to these climate variables, inclusive of their values up to two months prior to capture potential memory effects (e.g. in moisture) and lagged ecosystem responses. We then use the first two principal components (PCs), also interpreted as explanatory climate components of regional climate variability and change (figure 3(b)), in our LAI regression. The PCA preprocessing allows us to: (1) identify independent climate components for our regressions, and (2) reveal how these components are comprised of the interacting climate variables. The latter is important because recent work (Adole *et al* 2016, 2019) highlight how interactions between moisture and temperature mediate vegetation responses across Africa, even in water-limited domains. We then regress LAI on these PC climate variables to investigate their contributions to the LAI Trend and the overall LAI signal (equation (4)).

Specifically, to assess the importance of the respective PC1 and PC2 climate Trends to the overall LAI timeseries, we further fit the PC regression by using EEMD to remove the Trend component from PC1 while keeping PC2 fully intact (equation (5)) and vice versa (equation (6)):

$$LAI_{month} \sim PC_1 + PC_2 + const., \tag{4}$$

$$LAI_{month} \sim PC_{1,IMF} + PC_2 + const., \tag{5}$$

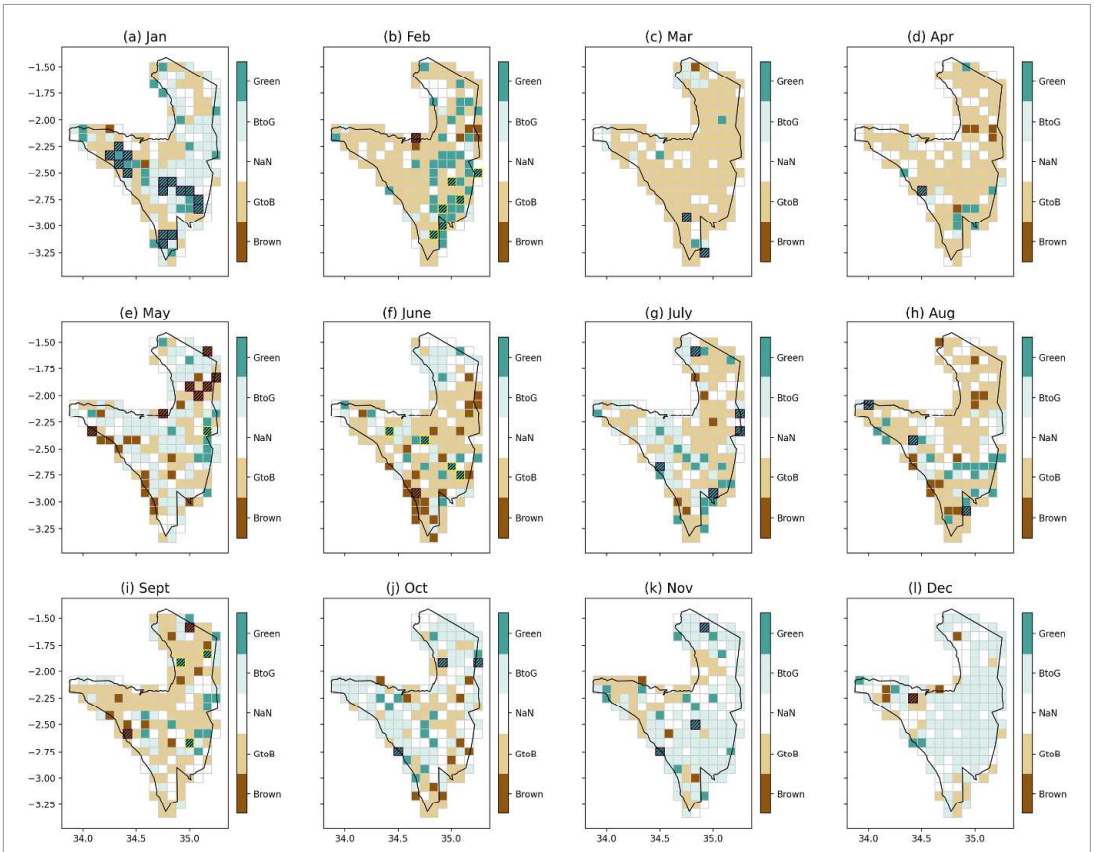

Figure 4. Monthly plots of LAI3g Trend categorization: Brown = monotonic browning; GtoB = reversal from greening to browning; BtoG = reversal from browning to greening; Green = monotonic greening; NaN denotes the remaining Trend has more than one extrema and cannot be classified in any of these categories; overplotted on some grid cells is black hatch lines, denoting that our surrogate test indicates the monotonic greening or browning Trend is significant at 0.05 level.

$$LAI_{month} \sim PC_1 + PC_{2,IMF} + const. \quad (6)$$

Finally, we evaluate how Trends from these climate variables affect the LAI Trend using the standard multiple EEMD-Regression (Yang *et al* 2011, Masselot *et al* 2018):

$$LAI_{month,Trend} \sim PC_{1,Trend} + PC_{2,Trend} + const. \quad (7)$$

3. Results

3.1. Time-varying changes to seasonal LAI

From 1982 to 2016, SNP LAI exhibits slight greening-to-browning Trend reversals and monotonic greening Trends at the annual and wet season temporal scales (figure E2), respectively. However, climate change and its interaction with modes of climate variability may have distinct impacts at monthly timescales (Nicholson *et al* 2017), which could further impact vegetation responses. Therefore, we further examine time-varying SNP LAI Trends for each month using the EEMD approach described in section 2.3 (see figure 3(a)). Firstly, there exists large spatial variation in the LAI Trend categorization across months, particularly during the dry season (June–October) (figure 4). Moreover, there is a lack of widespread significant monotonic Trends (indicated by black hatch lines) across the domain and months. Nevertheless, browning-to-greening and greening-to-browning Trend reversals are spatially widespread during November–December in the short-rains (figures 4(k) and (l)) and in March–April of the long-rains (figures 4(c) and (d)), respectively. These responses differ markedly from those indicated by a simple Mann–Kendall test (figure C1), as has been used in prior work (e.g. Chen *et al* 2019, Cortés *et al* 2021), which show more widespread greening trends (especially during the wet season from January to April) and significant gridcells.

Furthermore, while there are few significant monotonic Trends in monthly mean SNP LAI, the intra-annual LAI variability, i.e. the relative range defined as RREL = (max–min)/mean (Pettorelli *et al* 2012), does show widespread and significant monotonic increases (black hatching, per a Mann–Kendall test) over the 1982–2016 period. This measure captures the LAI amplitude during the annual and wet season cycles. This enhanced intra-annual variability is particularly concentrated in the southern and eastern areas (figure C2) of the domain which are broadly dominated by herbaceous vegetation and shrubs.

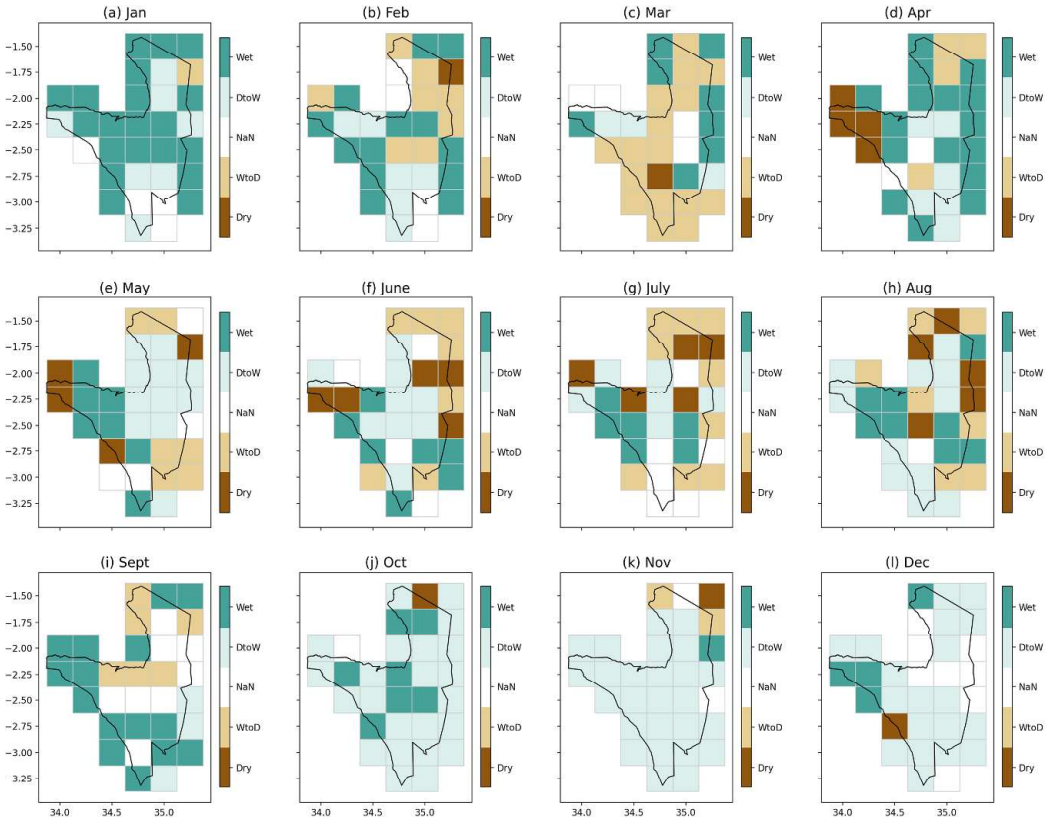

Figure 5. Monthly plots of GLEAM soil moisture Trend categorization: Dry = monotonic drying; WtoD = reversal from wetting to drying; DtoW = reversal from drying to wetting; Wet = monotonic wetting; NaN denotes the remaining Trend has more than one extrema and cannot be classified in any of these categories.

Yet, the timing of LAI maximum and minimum still displays large interannual variability without clear trends (figure C3). We provide context for this response in section 4, although a quantified attribution is beyond the scope of our analysis.

We also examine the timing of the prevailing LAI Trend reversals (figures C4 and C5): Greening-to-browning Trend reversals in the long rains season emerge around 2001–2002 (darker brown grid cells on March and April maps in figure C6 and the reversal points in the area-aggregated figures C5(g) and (h)). In contrast, the browning-to-greening that characterizes much of the short rains occurs in the late 1980s/early 1990s (figures C5(k) and (l)). We note that for the short rains, November and December, the VCRs (or the amount of total LAI variance the Trend captures) are relatively small (2.84%, 0.91%). March, in particular, exhibits the most uniform greening-to-browning across the domain with a comparatively higher 4.28% VCR.

3.2. The contribution of changing climate variables to SNP LAI change

The EEMD Trend categorization for soil moisture (figure 5) and precipitation (figure 6) reveal distinct responses during the individual months in the wet season, similar to the LAI results.

In November and December, the soil moisture and precipitation Trends (figures 5(k) and (l)) and 6(k) and (l)) show a drying-to-wetting and monotonic wetting Trend, respectively, which is consistent with prior work (Nicholson *et al* 2017, Bartzke *et al* 2018). These moisture Trends are broadly consistent with browning-to-greening during these months (figures 4(k) and (l)). We also note increased October precipitation (figure 6(j)) and drying-to-wetting Trends in soil moisture (figure 5(j)), preceding the November/December LAI responses. The short rains Trend reversal for soil moisture occurs near the beginning of the time series (figure C7), similar to the timing of the browning-to-greening Trends in LAI (figure C6). Qualitatively, this suggests that the LAI increases during short rains (figures C5(g) and (h)) may be related to the largely co-occurring increases in moisture availability that begin early in the 1982–2016 period. We note however that the soil moisture dataset is more coarsely spatially resolved compared to LAI3g dataset, which limits comparative interpretations of reversal timings between these variables.

The potential relationships between LAI and the moisture variables appear more complicated during the long rains. There are widespread wetting-to-drying Trends in March for soil moisture (figure 5(c)) that are consistent with the greening-to-browning

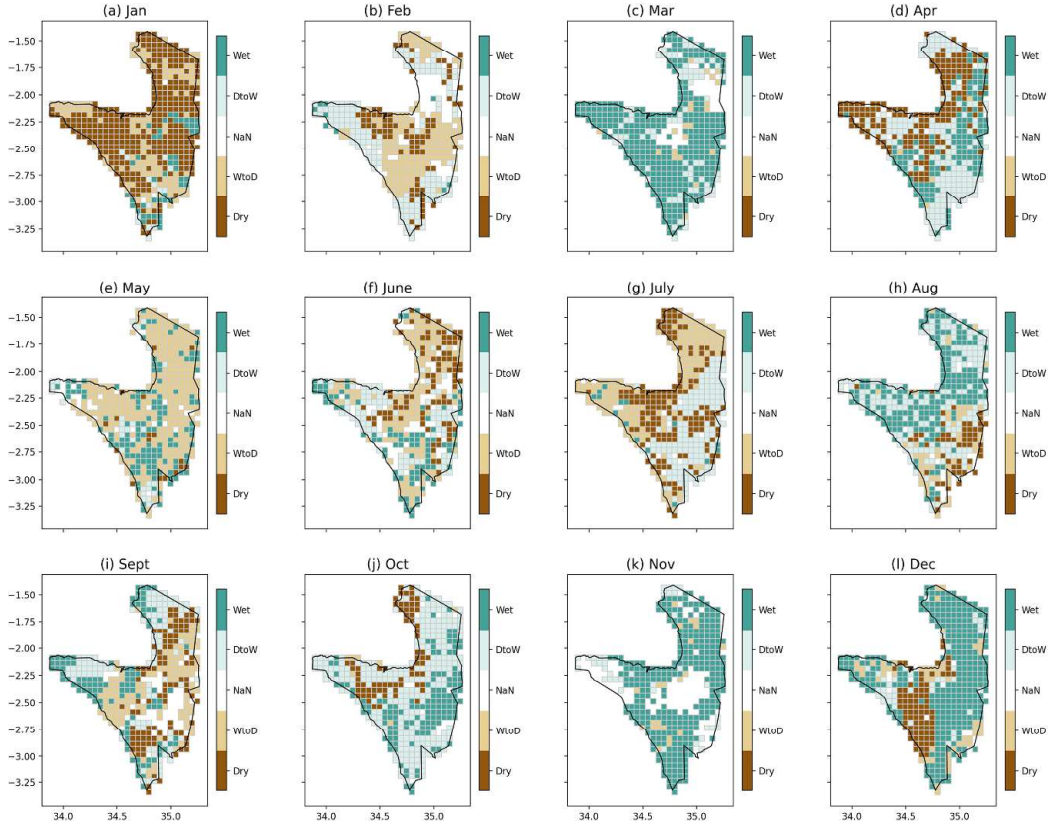

Figure 6. Monthly plots of CHIRPS precipitation Trend categorization: Dry = monotonic drying; WtoD = reversal from wetting to drying; DtoW = reversal from drying to wetting; Wet = monotonic wetting; NaN inside the SNP polygon denotes the remaining Trend has more than one extrema and cannot be classified in any of these categories.

LAI Trends (figure 4(c)). However, the wet season precipitation Trends are less temporally coherent with these LAI and soil moisture Trends, particularly from January to April. March (figure 6(c)) largely shows monotonic increases in precipitation throughout much of the domain, while January and February (figures 6(a) and (b)) show monotonic declines and wetting-to-drying reversals in precipitation, respectively. In contrast, soil moisture largely shows increasing Trends over nearly the entire SNP in January and much of the domain in February (figures 5(a) and (b)). Qualitatively, this may indicate a potentially lagged relationship between precipitation and LAI Trends in the long rains, as mediated through soil moisture.

Given this response, we evaluate more explicitly the possible (lagged) relationships between the climate variables and LAI using PC-Regression and EEMD-Regression techniques (section 2.4, figure 3(b)). We focus our regression analyses on better characterizing the March LAI response during the long rains, motivated by its spatially widespread greening-to-browning Trend reversals and relatively high VCR (figure 4(c)).

Our PC analysis (figure 3(b)) shows that PC1 loads heavily on soil moisture and precipitation while PC2 loads more strongly on temperature (table D1). We therefore interpret these as the 'moisture' and 'temperature' components (of regional climate variability and change), respectively. Furthermore, moisture variables in January and February display relatively strong correlations with March LAI (figure D3), supporting a lagged relationship between moisture availability and early long rains green-up, and are also important components of the PCs (table D1). PC-regression results (tables 2 and 4) indicate both PC1 and PC2, i.e. the moisture and temperature components combined, are significant and explain March LAI moderately well (adj. $R^2 = 0.6$). Sensitivity analyses (figure 7(a)) show that the detrended moisture component (table 2, equation (5)) yields a worse model than the detrended temperature component (table 2, equation (6)), evidenced by lower adjusted R^2 and worse AIC/BIC scoring criteria. This suggests that the moisture Trend is more important than the temperature Trend for predicting the overall March LAI. Nevertheless, Trends belonging to both the moisture and temperature components are highly important to explain the greening-to-browning Trend reversal in March LAI, evidenced by the good fit in EEMD Trend Regression (adj. $R^2 = 0.975$) and their statistical significance (table 2, figure 7(b)).

Table 2. Results from OLS Regression of March LAI.

Modality	Equation	Adj. R^2	AIC	BIC	Significant covariates[1]
PC-R	(4)	0.626	3.753	8.419	PC1 (+), PC2(−)
PC-R	(5)	0.557	9.697	14.36	PC1_IMF (+)
PC-R	(6)	0.611	5.173	9.839	PC1 (+), PC2_IMF (−)
EEMD-R Trend	(7)	0.975	−209.9	−205.2	PC1_Trend, PC2_Trend[2]

[1] Significance level at 0.05, +/− for positive/negative coefficients.

[2] Due to high multicollinearity, the coefficients are biased and their signs are omitted to avoid misinterpretation.

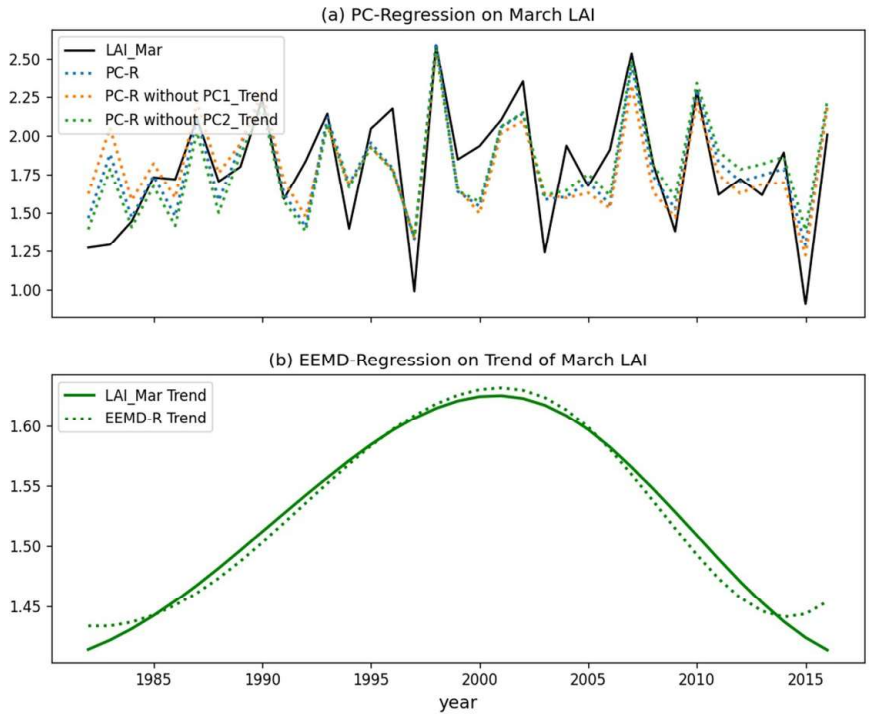

Figure 7. Regression results on March LAI: (a) PC-Regression with counter-factuals, (b) EEMD-Regression for Trend. Plot (a) shows both moisture and temperature variables are significant to overall March LAI signal. Plot (b) shows the March LAI Trend is well-fitted by the Trends from climate variables. The March LAI series and its decomposed Trend are shown in solid lines, while the regression fitted values are shown in dotted lines.

4. Discussion

Our results show no linear declines in 1982–2016 annual SNP LAI (figure E1(a)), which contrasts with earlier work suggesting climate-change driven declining annual NPP, or NDVI, over the approximate SNP area during this period (Pettorelli *et al* 2012, Kalisa *et al* 2019). Our findings are more consistent with studies showing nonlinear annual trends at larger (Wei *et al* 2018) and aggregated (Kalisa *et al* 2019) spatial scales encompassing all of East Africa. Furthermore, while these studies indicate that browning emerges in the overall LAI signal around the year 2000, our analysis of the SNP LAI Trend alone shows minimal change post-2000.

Nevertheless, at sub-seasonal and monthly timescales, our results do reveal distinctive, and spatially homogenous, nonlinear SNP vegetation Trends: specifically, a browning-to-greening in the short rains (November–December) starting in the late 1980s/early 1990s and a greening-to-browning in March–April in 2001–2002. Furthermore, when measured from their inflection points, the approximately linear browning trend in March is around 0.1 m^2/m^2/year (figure C5(g)) and the November/December greening (figures C5(k)/(l)) is 0.08–0.1 m^2/m^2/year. While we did not find similar monthly analyses against which to compare these Trends, they are generally comparable in magnitude to the global, growing-season trends reported by other studies, such as approximately 0.07 m^2/m^2/year reported by Zhu *et al* (2016).

These findings demonstrate the utility and importance of high-resolution, spatially-explicit, sub-seasonal and monthly analyses for assessing climate change-ecosystem interactions, particularly in

protected areas where land use change is, ostensibly, minimal (Pelkey *et al* 2003, Nicholson *et al* 2017). Our EEMD and surrogate testing approach captures nonlinear Trends without the restrictive assumptions of the Mann–Kendall Test (e.g. serial-independence), which has been previously used to assess vegetation trends in Africa and globally (Pettorelli *et al* 2012, Chen *et al* 2019). Importantly, our approach is a robust procedure that minimizes false positive trends, which have resulted from simpler approaches to evaluate vegetation greening effects (Cortés *et al* 2021).

To identify climate influences on mean SNP LAI Trends, our combined PCA and EEMD regressions move beyond simply correlating LAI and climate variables, and are unique in explicitly capturing interactions between climate variables and their lagged SNP LAI impacts. A novel finding of this approach is the importance of both SNP moisture and temperature Trends to the SNP March LAI Trend, as well as the interaction between these climate variables (and their lags) evidenced by their loading in both PCs. Increasing water limitation in March across the SNP, i.e. soil moisture declines that lag declining January and February precipitation Trends, and rising temperature Trends across these months all contribute to March browning. To our knowledge, this is the first analysis of how interacting climate variables, both in their monthly lagged effects and Trends, contribute to subseasonal vegetation variability and Trends in SNP.

These findings align with previous work suggesting that interactions between moisture, temperature, and other physical variables shape intra-seasonal vegetation phenology across Africa writ large (Ryan *et al* 2017, Adole *et al* 2018, 2019). The browning-to-greening during the short rains likely results from increasing precipitation that enhances soil moisture, which we also show (figures 5 and 6) and has previously been reported around the SNP (Ogutu *et al* 2008, Bartzke *et al* 2018), although these studies did not focus on subsequent impacts to vegetation. Notwithstanding important moisture-temperature interactions, our findings that moisture availability and memory are strong determinants of SNP vegetation responses is generally consistent with our understanding of water-limited African ecosystem dynamics (Zhang *et al* 2005, 2006, Wei *et al* 2018, Adole *et al* 2019).

In addition, our findings of increasing intra-annual LAI variability from 1982 to 2016 is consistent with NPP analyses by Pettorelli *et al* (2012), averaged for the SNP domain. Our spatially-explicit analysis further reveals that this increasing variability occurs in predominantly herbaceous vegetation- and shrub-dominated eastern and southern SNP. As this study primarily focused on identifying mean LAI Trends and their drivers, attributing these long-term changes in intra-annual LAI variability is beyond our scope. We nevertheless suggest that increasing precipitation variability is likely to play a role. For example, prior studies suggested that regional precipitation may be displaying more intra- and inter-annual variability (Bartzke *et al* 2018), partly relating to changing Indo-Pacific sea surface temperatures and subsequent impacts to regional atmospheric circulation and moisture transport (e.g. Williams and Funk 2011, Nicholson *et al* 2017). Future work using process-based Earth system and/or ecosystem models (e.g. Liu *et al* 2015) that include (African) vegetation sensitivities to a range of climate variables (Adole *et al* 2018, 2019) could better isolate natural variability versus anthropogenic versus forcings to attribute change in multiple SNP vegetation characteristics.

Global and larger-scale regional studies of greening and browning may obscure or even overestimate important vegetation trends in protected areas, where climate change poses an increasing threat (Mondal *et al* 2020). Our results augment the increasing body of work on East African ecosystems to show that SNP vegetation Trends are nonlinear, and thus require regular monitoring and rigorous evaluation at fine spatial and temporal scales to tease out the many sources of variability, inclusive of climate change. Indeed the long-term monitoring and evaluation of vegetation (and ecosystem) health may be just as important for biodiversity and conservation goals, e.g. Sustainable Development Goal 15: Life on Land, as the amount of area protected (Sinclair *et al* 2008, UN 2015, Elsen *et al* 2020). While the monthly LAI Trends we identify account for a relatively small portion of the overall inter-annual vegetation variability, our results nevertheless reveal contrasting Trends between the short and long rains. Along with enhanced intra-annual LAI variability, these differences may influence ecosystem phenology and dynamics (Scheffers *et al* 2016, Elsen *et al* 2020) as 'slow changes and trends' (Sinclair *et al* 2008). For example, monthly vegetation Trends and their differences between the short and long rains may incite shifts in the timing and locations of herbivore migration, contributing to changing food web dynamics (Ritchie *et al* 2008).

We further note limitations to this study that complicate a comprehensive attribution of these LAI Trends and climate variables. Firstly, prior work comparing different LAI products demonstrates that different Trends and responses may emerge depending upon the product used (Zhu *et al* 2016). Therefore, evaluating agreement across products is critical to assessing vegetation changes, particularly in protected ecosystems with relatively small area footprints (∼15%) and where widespread, frequent ground monitoring is not always available.

Secondly, we note that our two-step approach of PCA followed by EEMD-Regression does not exclude possible multicollinearities between the IMFs of each PC, which could limit the statistical test power on the covariates in EEMD-Regression. One might consider

a more flexible model that does not impose assumptions on independent covariates and better capture their interactions. Regardless, advanced statistical methods to identify climate change impacts on SNP vegetation should focus on interpretability while also capturing important interactions between climate variables.

Lastly, previous studies have documented changes across a host of other important abiotic and biotic determinants of Serengeti ecosystem dynamics. Among the most impactful is increasing human land use around the greater Serengeti-Mara ecosystem, which includes the SNP, that may threaten SNP ecosystem dynamics and functionality (Sinclair *et al* 2008, Li *et al* 2010, Estes *et al* 2012, Byrom *et al* 2015, Probert *et al* 2019, Veldhuis *et al* 2019, Kija *et al* 2020). For example, reductions in fire and habitat degradation due enhanced grazing and agricultural activities are likely facilitating changing vegetation distributions that incite further changes in SNP species composition, dynamics, and ecosystem biogeochemical interactions (Dublin and Ogutu 2015, Green *et al* 2019, Nkwabi *et al* 2019, Probert *et al* 2019, Veldhuis *et al* 2019). Our methods are not constructed to directly disentangle climate change from these other strong SNP determinants. Future work should thus seek to further control for land use change when evaluating the role of climate change on vegetation in the SNP.

5. Conclusions

SNP is a critical hotspot of biodiversity, characterized by complex ecosystem dynamics and intensifying human pressures, including land use and climate change. We conducted rigorous analyses using EEMD to identify sub-seasonal, spatially-explicit Trends in widely-used remote sensing datasets of leaf area, precipitation, temperature, and model-produced soil moisture in the SNP from 1982 to 2016. We further employed novel PCA and regression techniques to determine how temperature and moisture variables, and their lagged interactions, contribute to these trends. We found long-term SNP Trends to be nonlinear, with spatially-uniform greening-to-browning during March and browning-to-greening during November–December. While the SNP ecosystem is water-limited, both moisture and temperature Trends, and their values from January–March, were critical to explain March greening-to-browning vegetation Trends. Our findings demonstrate the importance of evaluating long-term ecosystem trends in the SNP at monthly timescales, when vegetation responses can differ substantially, and of including multiple, interactive climate variables in attributing these vegetation changes.

Data availability statement

No new data were created or analysed in this study.

Acknowledgments

The authors would like to acknowledge the NYU Center for Data Science and the Moore-Sloan Data Science Environment (MSDSE) for providing funds for Teresa Huang's work on this project. We would also like to thank Dustin Braden at the University of Delaware and Jessica Clark who was supported by the Center for Food Systems and Sustainability at the University of Delaware.

Appendix A. Main manuscript section 2.1: Serengeti National Park (SNP)

Average annual precipitation in the SNP is highest in the northern and western regions (figure A1(c)). The spatial pattern of average annual soil moisture is consistent with precipitation (figure A1(b)), highest in the northern SNP corresponding well with the regional maximum in LAI. Annual average temperatures are less variable over the domain (figure A1(d)). The highest temperatures occur in the central and western areas, while slightly cooler conditions prevail in the east and north.

For completeness, we compare LAI3g with MCD15A3H Version 6 Moderate Resolution Imaging Spectroradiometer Level 4 LAI (MODIS LAI) (Myneni *et al* 2015), GLASS LAI From Time-Series MODIS Surface Reflectance (GLASS) (Liang *et al* 2013), and NOAA Climate Data Record of AVHRR LAI (CDR) (Claverie *et al* 2016). MODIS LAI is a 4-day composite data set with 500-meter pixel size. It chooses the best pixel available from all the acquisitions of both MODIS sensors located on NASA's Terra and Aqua satellites from within the 4-day period. GLASS is an 8-day composite data with 0.05-degree resolution. It generates one-year LAI estimates by fitting general regression neural networks on one-year MODIS Surface Reflectance data, which improves quality by considering the temporal pattern (Xiao *et al* 2017). CDR is a daily composite data with 0.05-degree resolution, derived from the NOAA AVHRR Surface Reflectance product. CDR estimates LAI values globally over land surfaces, but not over bare or very sparsely vegetated areas, which results in several grid cells of missing data within our defined SNP domain. Brief descriptions and references for all four LAI products considered for our analyses are given in table 1. MODIS LAI and CDR datasets are queried from Google Earth Engine while LAI3g and GLASS are downloaded from source webpages.

To evaluate agreement between LAI products, we first compare their temporal patterns shown in figure A2. The mean values for each data product time series are calculated by averaging all the grid cells with centroids overlapping the SNP polygon at the respective time interval. Although MODIS LAI only has data available from 2002 and such short

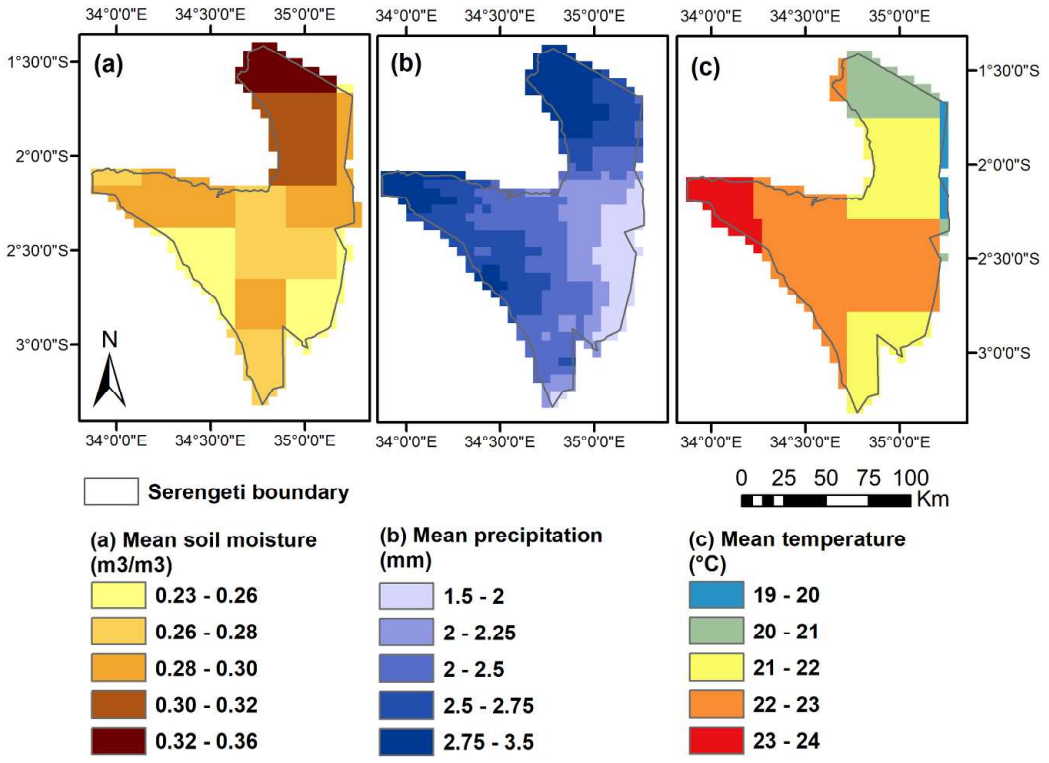

Figure A1. Time-averaged (2003–2016) SNP attributes. (a) Root zone soil moisture, (b) precipitation, and (c) surface temperature. Values for (a) is from GLEAM, (b) from CHIRPS, and (c) from CRU TS monthly high-resolution gridded surface temperature dataset (CRU TS) (product details in table 1).

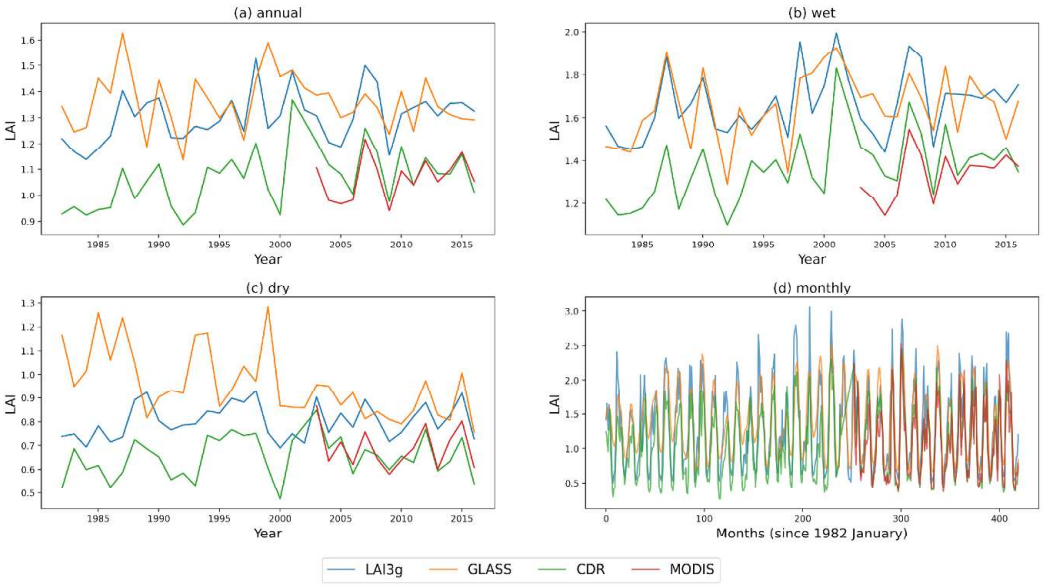

Figure A2. Temporal patterns for four different products (LAI3g; GLASS; CDR; and MODIS LAI) evaluated in this study for the SNP spatial-aggregated mean at (a) annual, (b) wet season, (c) dry season, and (d) month level.

time frame is not suitable for our long-term trend study, it is a high quality dataset with the finest spatial resolution (of those products considered here) and relatively less measurement uncertainty (Fang *et al* 2013). Therefore, we conduct a set of spatial and temporal correlation analyses using the MODIS LAI as a 'benchmark' to assess how similar these LAI products are both to MODIS LAI and to each other, during their overlapping periods. We employ the Spearman rank correlation test here as it is suitable for

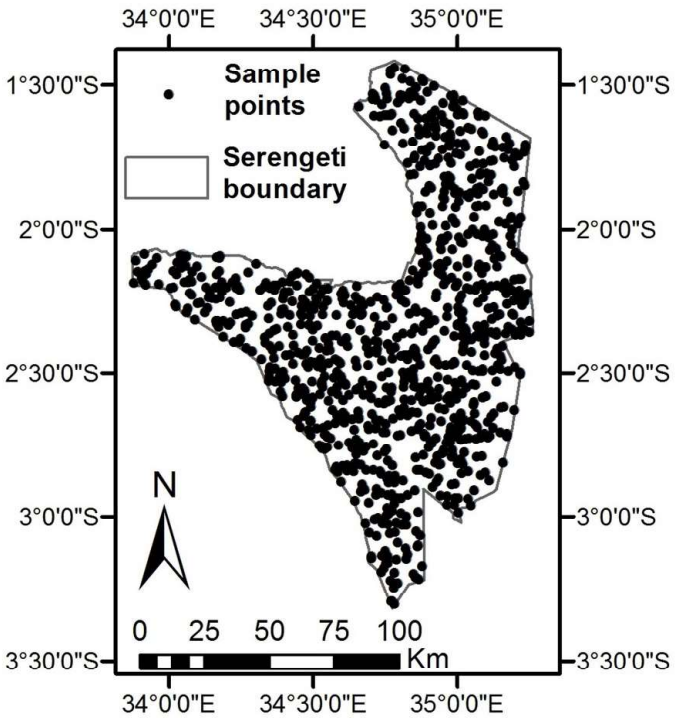

Figure A3. 1000 sampling points from SNP, used to calculate the spatial correlation among LAI products.

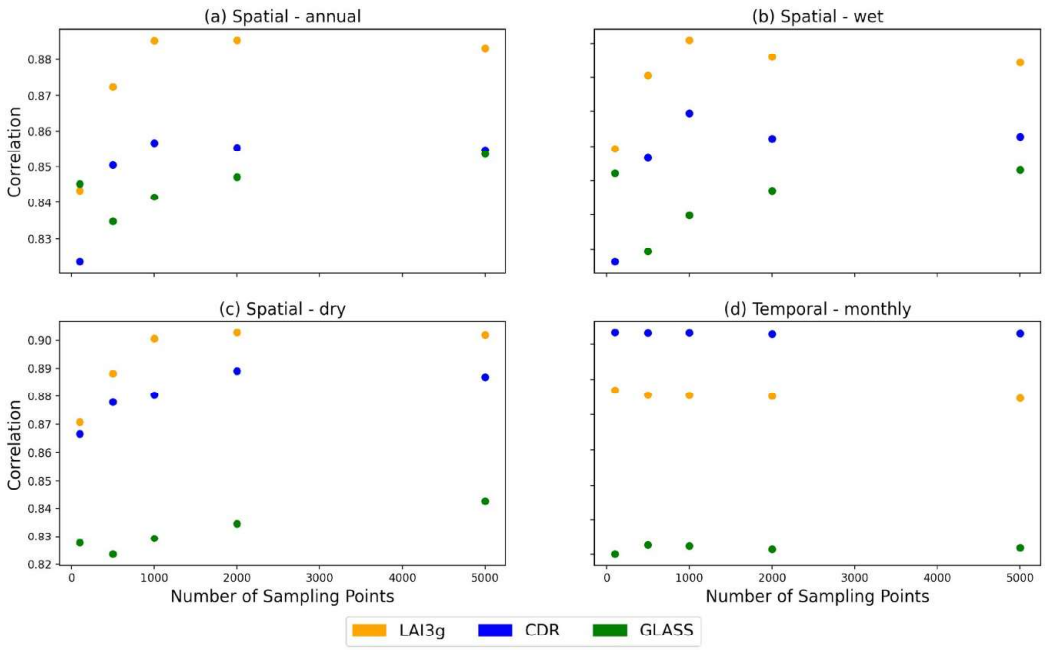

Figure A4. Spearman Rank Correlation with MODIS LAI among products for varying number of sampling points. (a)–(c) show the result of spatial correlation and (d) shows the result of temporal correlation.

nonlinear data, and this analysis enables us to identify which LAI product may be best suited for our analyses to detect long-term trends changes.

To standardize our correlation analysis in the temporal dimension, we first compute the monthly mean for each product (16 years × 12 months) spatially aggregated over the domain for each point in time. Given the variation in geospatial resolutions of the LAI datasets used, we adopt the following sampling strategy for assessing the products' spatial

Table A1. Spearman rank correlation with MODIS LAI for CDR, LAI3g and GLASS, under different number of sampling points.

Product	Spatial: annual	Spatial: wet	Spatial: dry	Temporal: monthly	Sample size
CDR	0.823	0.796	0.867	**0.966**	100
LAI3G	0.843	**0.829**	**0.871**	0.934	100
GLASS	**0.845**	0.822	0.828	0.840	100
CDR	0.851	0.827	0.878	**0.966**	500
LAI3G	**0.872**	**0.850**	**0.888**	0.931	500
GLASS	0.835	0.799	0.824	0.845	500
CDR	0.857	0.839	0.880	**0.966**	1000
LAI3G	**0.885**	**0.861**	**0.900**	0.931	1000
GLASS	0.842	0.810	0.829	0.845	1000
CDR	0.855	0.832	0.889	**0.966**	2000
LAI3G	**0.886**	**0.856**	**0.903**	0.930	2000
GLASS	0.847	0.817	0.835	0.843	2000
CDR	0.855	0.833	0.887	**0.966**	5000
LAI3G	**0.883**	**0.854**	**0.902**	0.929	5000
GLASS	0.854	0.823	0.843	0.844	5000

correlation: we first draw N random points (varying over $N \in \{100, 500, 1000, 2000, 5000\}$, figure A3) uniformly from the SNP domain using 'rejection sampling'. Specifically, we define a rectangular boundary by the minimum and maximum of x-axis and y-axis in SNP polygon, and then generate a point within this rectangle selecting those that specifically fall within the SNP polygon. Points are generated until the total number of points equals N. The spatial correlation is then computed using the N sampling points for the annual or seasonal mean. We find that $N = 1000$ is a satisfactory number of sampling points, after which the improvements in correlation cease and we risk duplicating sampling points in coarser products (such as LAI3g). The spatial distribution of these 1000 sampling points, shown in figure A3, does well to represent the SNP domain.

Figure A4 and table A1 present the spatial and temporal correlations results. Temporally, MODIS LAI is most closely correlated to CDR and LAI3g, but less so with GLASS. However, we note that CDR has several missing values over the SNP domain, which may complicate its use in this analysis. Spatially, however, MODIS LAI is more correlated to LAI3g, which is expected given that algorithms used to create the LAI3g dataset were calibrated and trained with respect to MODIS LAI (Zhu *et al* 2013). Given these considerations and correlative findings, we use LAI3g throughout our analysis to answer our research questions.

Appendix B. Main manuscript section 2.3: evaluating time-varying changes to seasonal LAI

We describe our surrogate hypothesis testing method for the nonlinear, monotonic EEMD Trend using iteratively refined amplitude adjusted Fourier transform method (IAAFT, (Schreiber and Schmitz 1996)).

Surrogate hypothesis testing (Theiler *et al* 1992) is a statistical approach to evaluate nonlinearity in timeseries data. Time series data is typically composed with long-term nonlinear determinism, short-term linear correlations, chaos and noise. To test for the significance of nonlinearity, the method first specifies some linear stochastic process as a null hypothesis, then generates surrogate data sets based on this null hypothesis, and finally computes a discriminating test statistic for the original and for each of the surrogate data sets. If the value computed for the original data is significantly different than those computed for the surrogate data, then the null hypothesis is rejected and significant nonlinearity is detected.

To test on nonlinear, monotonic LAI Trends, we need to specify our null model (which may be due to other sources of climate variability or other ecosystem dynamics). We assume the time series noise is generated from a linear stochastic process, and measured through a potentially nonlinear function. The null hypothesis is that the underlying process is from linear noise, while the alternative being a nonlinear deterministic trend.

We then apply IAAFT to generate surrogates using Fourier transform. Recall the key relationship between the time domain and the frequency domain: The linear correlations in the time domain are represented by the power spectrum amplitudes in the frequency domain, while the nonlinear correlations are captured in the phase angles. In light of this, the algorithm first computes the Fourier transform of the signal. Next, it randomizes the phase angles of the Fourier transformed signal so as to destroy any original nonlinearity, while preserving the amplitudes that capture original linear signals. It then reconstructs the surrogates through Inverse Fourier transform. Lastly, it corrects the spectrum and the distribution of the surrogate to align with the

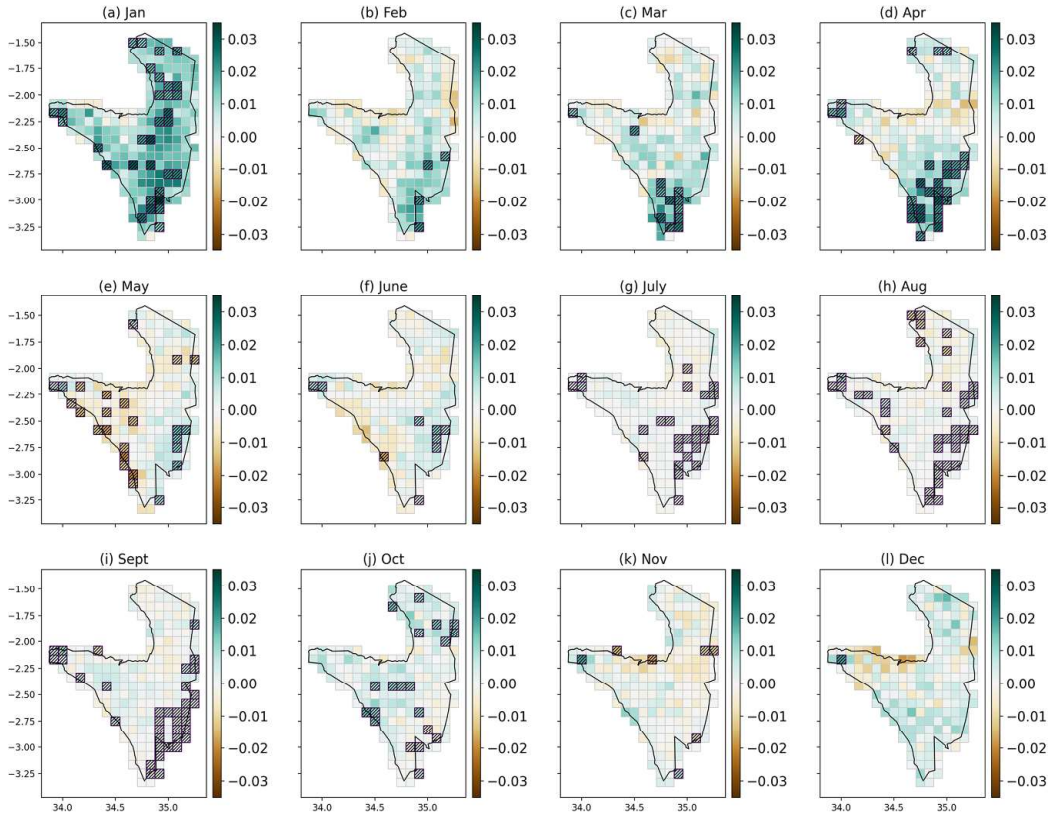

Figure C1. Monthly plots of LAI3g Mann–Kendall trends: brown indicates negative slopes while green indicates positive slopes; Overplotted on some grid cells is black hatch lines, denoting the greening or browning trend is significant at 0.05 level.

original signal, so as to avoid mixing potential nonlinear effects from the measurement function. In the end, IAAFT generates a surrogate that has same linear property as the original signal while randomizes the nonlinearity.

After generating the surrogates, we test the significance of the nonlinearity of the LAI Trend versus its surrogates by computing the test statistic. For a one-sided test, if the test statistic of LAI Trend is the maximum or minimum out of all K surrogates, then it yields a p-value of $1/(1+K)$. Here, we fix our p-value as 0.05 and thus generate $K = 19$ surrogates (Schreiber and Schmitz 1996).

Appendix C. Main manuscript section 3.1: changes and trends in interannual SNP LAI

For comparison, we perform Mann–Kendall trend test on SNP LAI. Figure C1 shows the monthly trend slope from 1982 to 2016 per grid cell over SNP. Contrary to the EEMD Trends, the Mann–Kendall trends display quite different patterns, with a predominantly greening trend in the wet season and more significant grid cells.

To identify the spatially-explicit changes in intra-annual LAI variability, we measure annual and wet season LAI variability using relative range: RREL = [MAX − MIN]/MEAN, where MAX, MIN, and MEAN are the annual or wet season maximum, minimum and mean LAI for each year during 1982–2016 (Pettorelli *et al* 2012). We then test for significant monotonic trend in the annual/seasonal LAI RREL using a Mann–Kendall trend test (MK test) (Kendall 1948, Pettorelli *et al* 2012). We compute RREL over the 1982–2016 period for the annual and wet season (November–May) (figure C2). The LAI RREL has been mostly increasing and a number of grid cells show significant monotonic trends. Earlier studies have also suggested domain-averaged increases SNP vegetation variability, (Ritchie *et al* 2008, Pettorelli *et al* 2012). Our results augment these previous findings to show that the increase in variability is predominantly in the eastern, central and south, parts of the domain, which are mainly characterized by grasses and shrubs.

To further evaluate SNP vegetaion variability, we compute the empirical distributions of the maximum

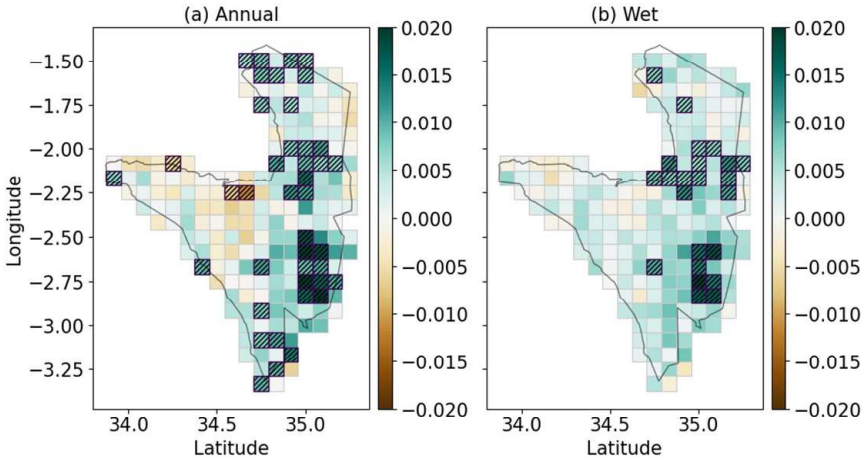

Figure C2. Intra-annual variability of LAI3g measured by Mann–Kendall trend test on relative range (RREL: (max–min)/mean in the given season). Green grid cells indicate positive slope from Mann–Kendall trend test, while brown grid cells indicate negative slope. Black hatch lines mark out grid cells with significant trend at 5% level.

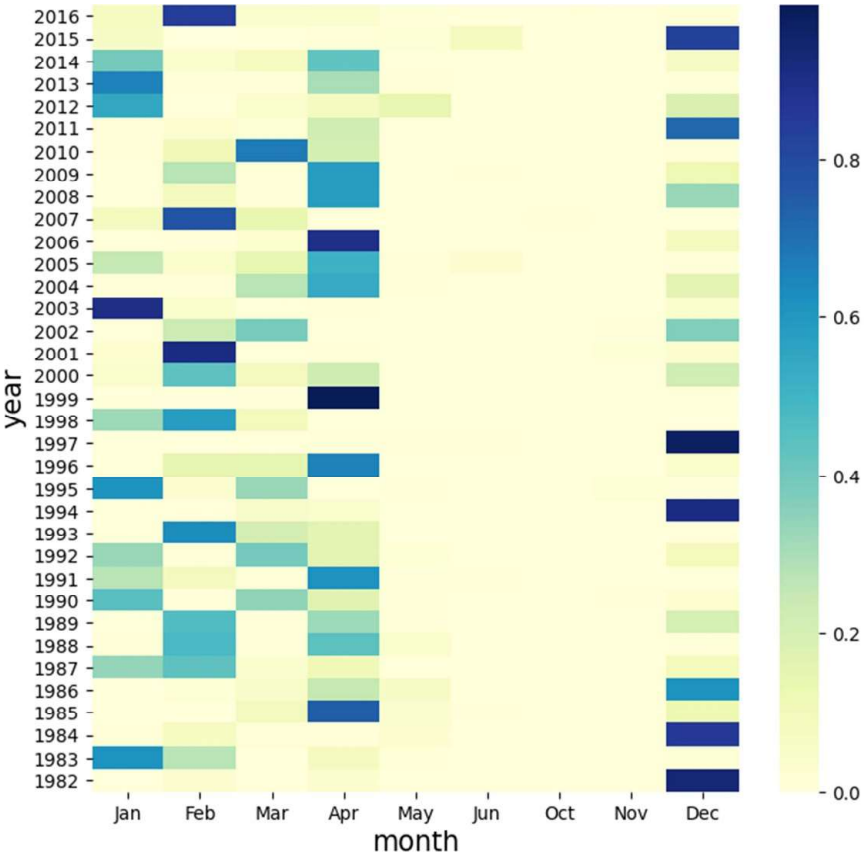

Figure C3. 1982–2016 Maximum LAI3g Timing Distribution (out of 196 SNP grid cells): For each year, we calculate the month that achieves peak LAI per pixel, and then aggregate them to compute the empirical distribution. Each grid cell represents the empirical probability of this month being the maximum out of all 12 months.

LAI timing from 1982 to 2016. As shown in figure C3, the timing of peak LAI in SNP varies drastically in different years.

To evaluate the validity of monthly time-scale of LAI response, we use bi-weekly LAI3g data to perform EEMD and Trend categorization during the wet season. As shown in figure C4, the Trend categorization remains largely the same between the first half and the second half of each month during the wet season, except May. These bi-weekly patterns are

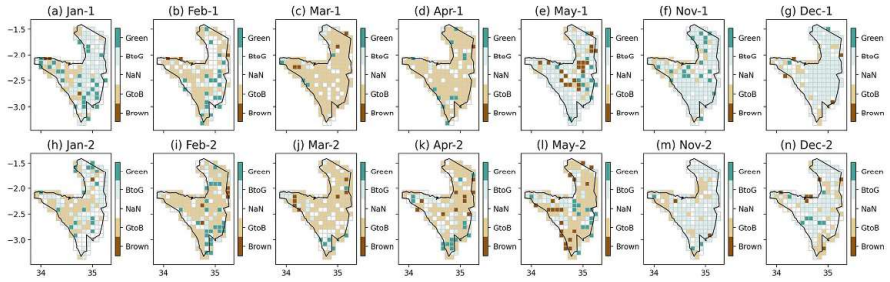

Figure C4. Bi-weekly plots of LAI3g Trend categorization: Brown = monotonic browning; GtoB = reversal from greening to browning; BtoG = reversal from browning to greening; Green = monotonic greening; NaN denotes the remaining Trend has more than one extrema and cannot be classified in any of these categories. Top (bottom) row shows the decomposed Trend from the first (last) two weeks of each month.

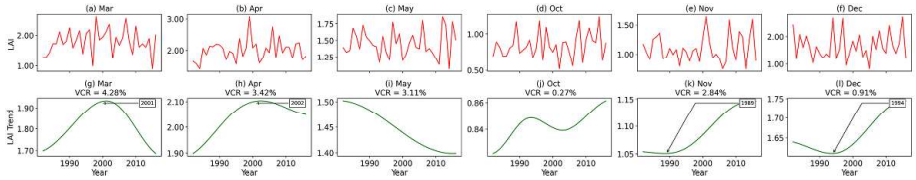

Figure C5. 1982–2016 LAI3g means for (a) March, (b) April, (c) May, (d) October, (e) November, and (f) December (1st row). EEMD decomposed Trend for (g) March, (h) April, (i) May, (j) October, (k) November, and (l) December (2nd row). Full monthly EEMD decomposition is available in figure E2. Also noted in (g)–(l) are the VCR values, which compare the variance of the LAI Trend to the overall variance of the original LAI timeseries in (a)–(f).

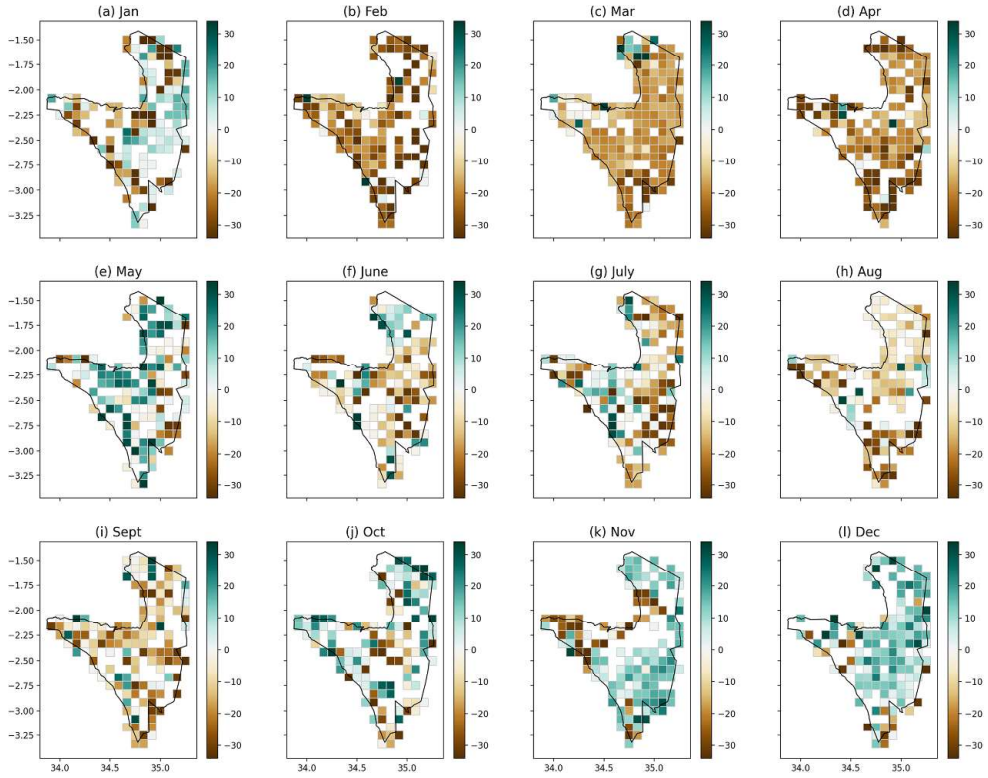

Figure C6. Inflection Year Pattern for LAI inflected Trends. Green indicates browning-to-greening Trends (denoted with positive values), and brown indicates greening-to-browning Trends (denoted with negative values). The absolute value of the pixel indicates the year of reversal in a numeric sequence, while the darker the color, the more recent the reversal point. Pixels with value 0 have more than one extrema.

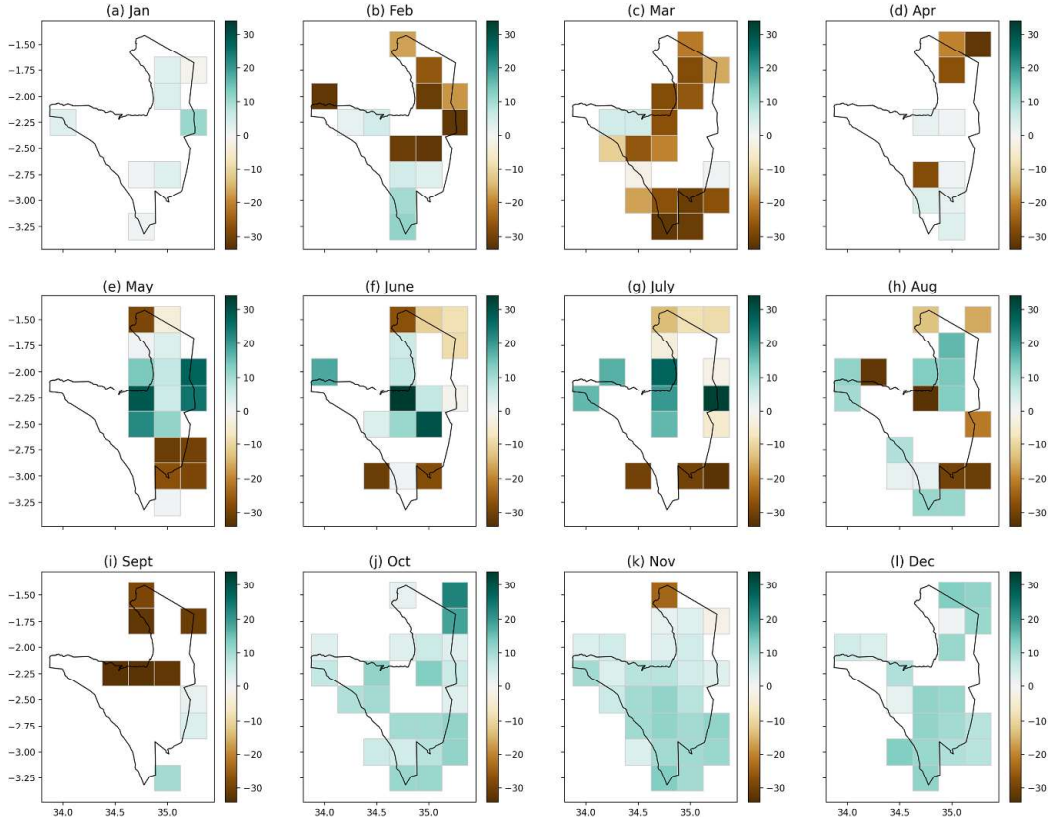

Figure C7. Inflection Year Pattern for soil moisture inflected Trends. Green indicates drying-to-wetting (denoted with positive values), and brown indicates weeting-to-drying Trends (denoted with negative values). The absolute value of the pixel indicates the year of reversal in a numeric sequence, while the darker the color, the more recent the reversal point. Pixels with value 0 have more than one extrema.

highly consistent with the monthly patterns shown in figure 4. Apart from the pure data-driven evidence, monthly response carries more distinct climate signals while finer time-scales could introduce more short-term climate noises. Hence, we rely on monthly responses in our analysis.

Consistent with figure 4, the trends on the spatial average of LAI over SNP domain show the similar reversal patterns. The VCR analysis suggests that the intrinsic trends are relatively subtle compared to the overall variability of LAI, which are largely driven by external forces such as climate factors.

Monthly maps (figures C6–C8) below indicate the timing of the reversal point revealed for each of the variables, LAI, soil moisture, and precipitation, using our EEMD analysis[7]. Gridcells shown are only for inflected trends, not for monotonic trends. Browning-to-greening reversals are denoted by positive values and greening-to-browning reversals are denoted by negative values. The absolute value of the pixel indicates the year of reversal in a numeric sequence, while the darker the color, the more recent the reversal point. For example, a dark blue value of +34 represents a browning-to-greening reversal point at year 2015, while a dark brown value of −34 represents a greening-to-browning reversal at year 2015. 0 means more than one extrema.

[7] In all the EEMD results, we set its stopping criteria as the absolute amplitude (max–min) of the remaining Trend is below 0.001, or its energy (sum of mean absolute difference) is below 0.005.

Appendix D. Main Manuscript section 3.2: the role of key climate variables in shaping interannual SNP LAI

Figures D1 and D2 show the soil moisture and precipitation means over SNP, together with the EEMD decomposed Trend, during the wet season months from 1982 to 2016.

To inform the quantitative regression modelling, we analyze the correlations between March LAI and the climate variables (figure D3) and their lags up to two months prior. Soil moisture, precipitation, and their lags up to January have high correlations with March LAI and there also exist moderately strong correlations between the climate variables.

We conduct PCA (section 2.4) to obtain the first two components (PCs) among the climate variables (table D1). PC1 loads most strongly on soil moisture and precipitation, indicating the importance of hydroclimate variation within this domain, while PC2

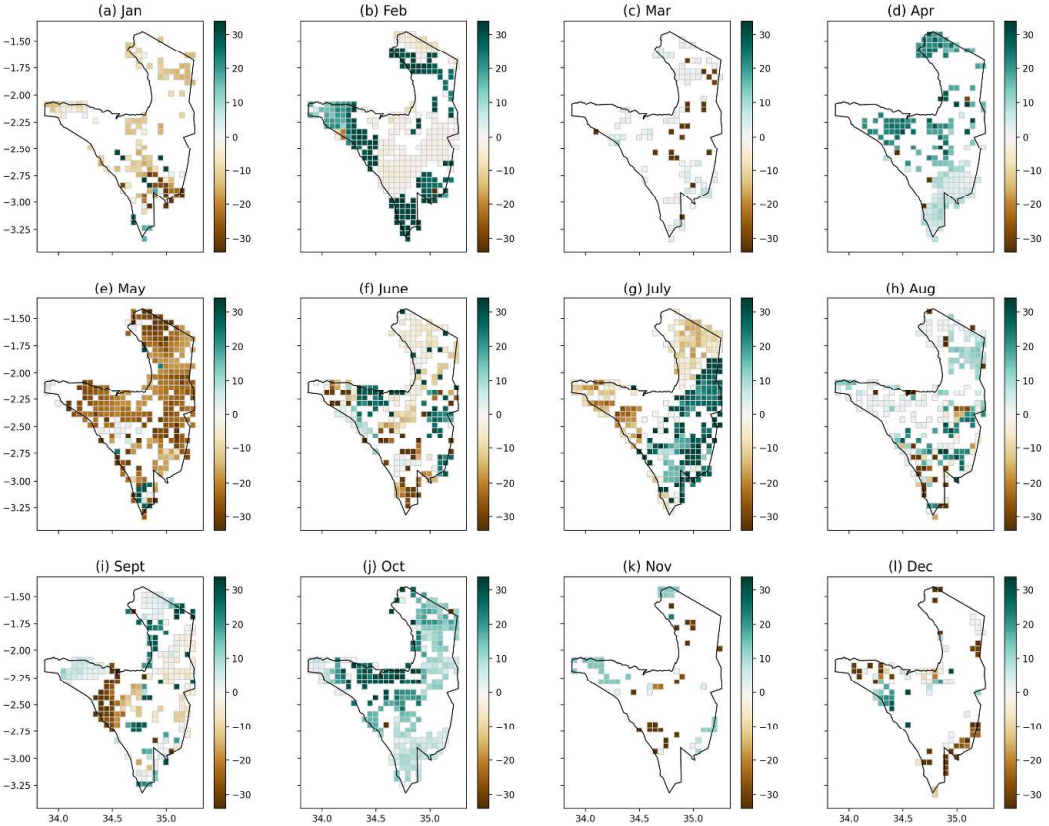

Figure C8. Inflection Year Pattern for precipitation inflected Trends. Green indicates drying-to-wetting (denoted with positive values), and brown indicates weeting-to-drying Trends (denoted with negative values). The absolute value of the pixel indicates the year of reversal in a numeric sequence, while the darker the color, the more recent the reversal point. Pixels with value 0 have more than one extrema.

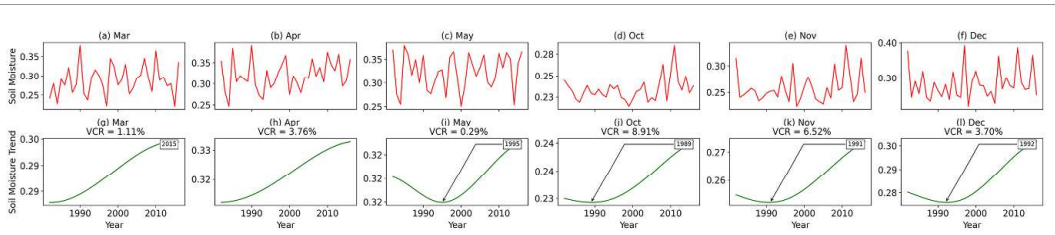

Figure D1. 1982–2016 GLEAM root zone soil moisture means for (a) March, (b) April, (c) May, (d) October, (e) November, and (f) December (1st row). EEMD decomposed Trend for (g) March, (h) April, (i) May, (j) October, (k) November, and (l) December (2nd row). Also noted in (g)–(l) are the VCR values, which compare the variance of the soil moisture trend to the overall variance of the original soil moisture timeseries in (a)–(f).

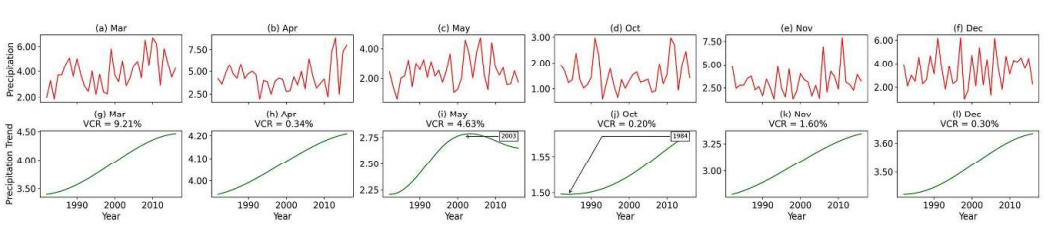

Figure D2. 1982–2016 CHIRPS precipitation means for for (a) March, (b) April, (c) May, (d) October, (e) November, and (f) December (1st row). EEMD decomposed Trend for (g) March, (h) April, (i) May, (j) October, (k) November, and (l) December (2nd row). Also noted in (g)–(l) are the VCR values, which compare the variance of the precipitation trend to the overall variance of the original precipitation timeseries in (a)–(f).

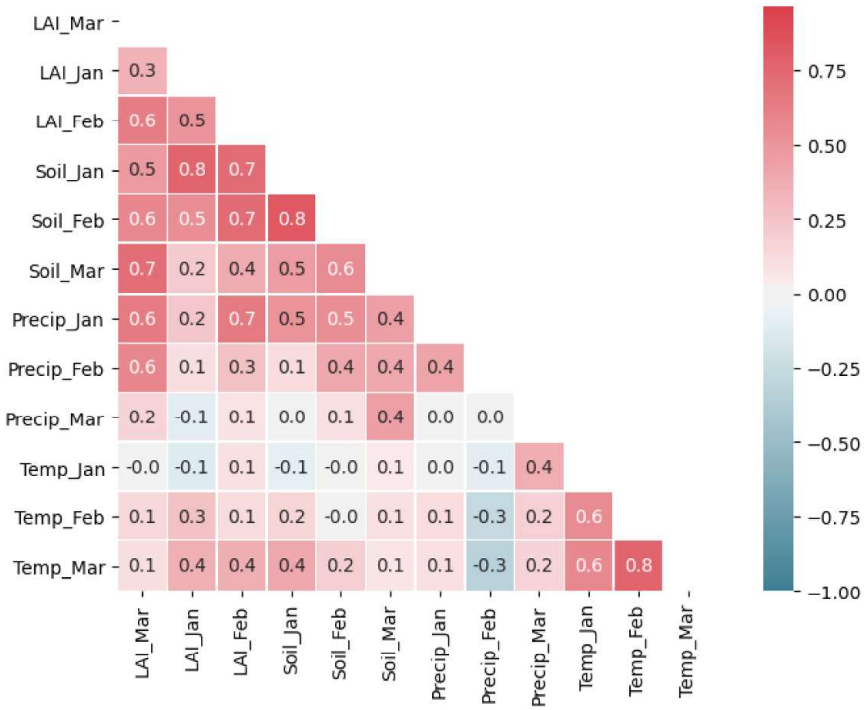

Figure D3. Correlation Heatmap of March LAI, it preceding months and climate variables.

Table D1. The loading matrix for the first two PCs. PC1 loads heavily on Soil and Precipitation, while PC2 is mostly driven by temperature, together with precipitation in February (negatively).

Driver	PC1	PC2
Soil_Jan	0.86	−0.09
Soil_Feb	0.90	−0.26
Soil_Mar	0.84	−0.18
Precip_Jan	0.71	−0.23
Precip_Feb	0.38	−0.63
Precip_Mar	0.24	0.28
Temp_Jan	0.25	0.81
Temp_Feb	0.31	0.86
Temp_Mar	0.40	0.80

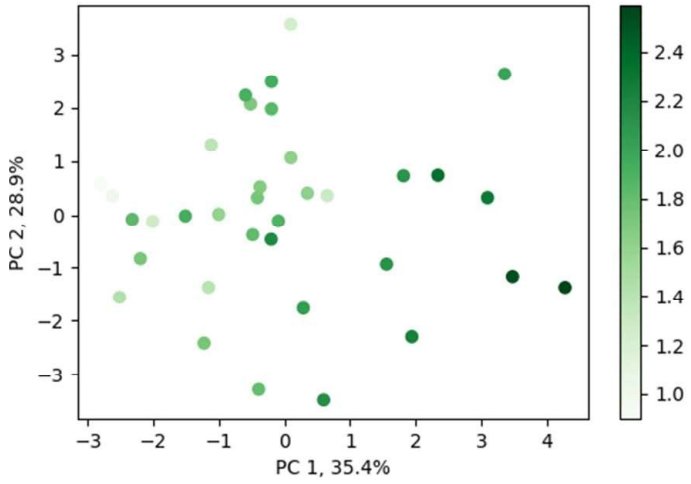

Figure D4. Projection of the climate variables data matrix (35 × 9) to the two-dimensional subspace spanned by the first two PCs. Points colored by LAI_Mar values.

Table D2. PC-R results (equation (4)).

Co-variate	Coefficients	P-value
PC1	0.169	0.000
PC2	−0.063	0.019

Table D3. PC1 Detrend results (equation (5)).

Co-variate	Coefficients	P-value
PC1_IMF	0.169	0.000
PC2	−0.034	0.239

Table D4. PC2 Detrend results (equation (6)).

Co-variate	Coefficients	P-value
PC1	0.160	0.000
PC2_IMF	−0.066	0.041

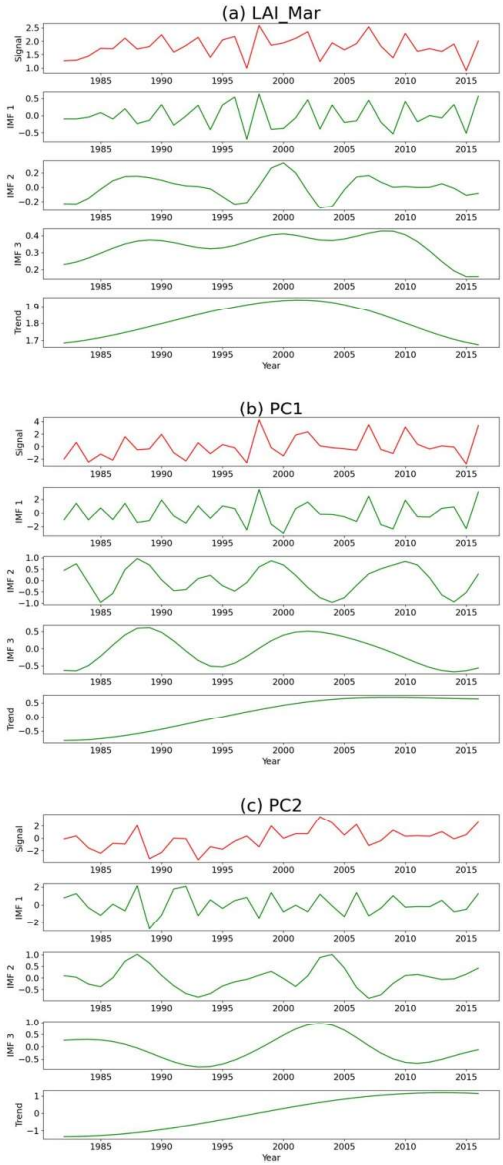

Figure D5. EEMD Decomposition of LAI_March (a), its PC1 (b) and PC2 (c) from the driver matrix. Interestingly, we can see PC1_Trend and PC2_Trend are very similar.

Table D5. EEMD-R Trend results.

LAI_Trend	Coefficients	P-value	VIF
PC1_Trend	0.685	0.000	28.225
PC2_Trend	−0.389	0.000	28.225
(Intercept)	1.469	0.000	

loads more strongly on temperature. We also note that Precip_Feb contributes strongly and negatively to PC2. We further illustrate the nine driver variables with 35 data points (i.e. 1982–2016) projected to the first two PCs, color-coded by March LAI values (figure D4). March LAI variation is mainly captured in the PC1 direction.

Tables D2–D4 show the results of PC-Regression (original), PC-R with detrended PC1, and PC-R with detrended PC2 respectively.

Figure D5 shows the EEMD for March LAI, its PC1 and PC2 from the driver matrix.

Table D5 shows the EEMD-Regression on Trend component: Trends from both PCs are highly significant. However, the high VIF factors indicates the multicollinearity issue between the covariates, and thus their coefficient values are biased due to confounding effects (Graham 2003).

Appendix E. Other supplemental figures

Below shows the full ensemble empirical mode decompositions for LAI in the SNP (using LAI3g), for annual/seasonal values (figure E1) and for each month (figure E2).

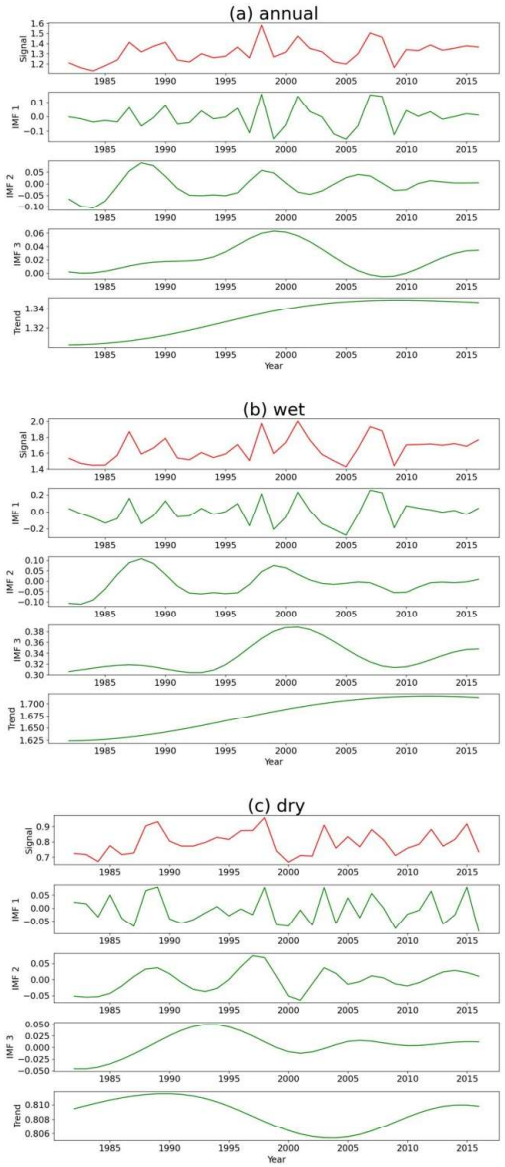

Figure E1. EEMD results for area-aggregated LAI3g time series for (a) annual, (b) wet and (c) dry seasons. For each subplot: the first row (red) shows the original area-aggregated LAI3g time series, each subsequent green row shows the IMF modes while the last row represents the remaining Trend.

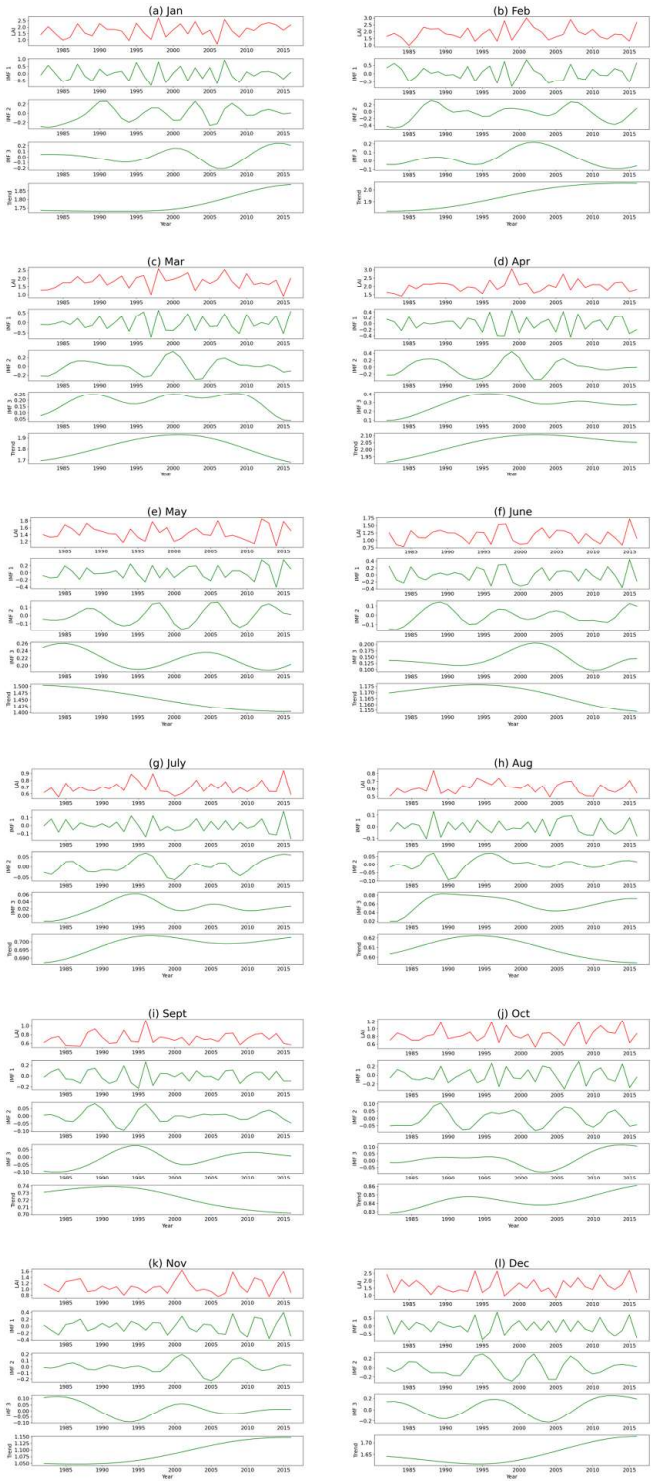

Figure E2. EEMD results for area-aggregated LAI monthly series over 1982–2016.

ORCID iDs

Ningyuan Huang https://orcid.org/0000-0001-6631-3737
Pinki Mondal https://orcid.org/0000-0002-7323-6335

References

Adole T *et al* 2019 Photoperiod controls vegetation phenology across Africa *Commun. Biol.* **2**

Adole T, Dash J and Atkinson P M 2016 A systematic review of vegetation phenology in Africa *Ecol. Inform.* **34** 117–28

Adole T, Dash J and Atkinson P M 2018 Large-scale prerain vegetation green-up across Africa *Global Change Biol.* **24** 4054–68

Bai L *et al* 2015 The regional features of temperature variation trends over Xinjiang in China by the ensemble empirical mode decomposition method *Int. J. Climatol.* **35** 3229–37

Bartzke G S *et al* 2018 Rainfall trends and variation in the Maasai Mara ecosystem and their implications for animal population and biodiversity dynamics *PLoS One* **13** e0202814

Byrom A E *et al* 2015 Anthropogenic stressors influence small mammal communities in tropical East African savanna at multiple spatial scales *Wildlife Res.* **42** 119–31

Camberlin P *et al* 2009 Components of rainy seasons' variability in equatorial East Africa: onset, cessation, rainfall frequency and intensity *Theor. Appl. Climatol.* **98** 237–49

Camberlin P and Okoola R E 2003 The onset and cessation of the "long rains" in eastern Africa and their interannual variability *Theor. Appl. Climatol.* **75** 43–54

Camberlin P and Philippon N 2002 The East African March-May rainy season: associated atmospheric dynamics and predictability over the 1968-97 period *J. Clim.* **15** 1002–19

Chen C *et al* 2019 China and India lead in greening of the world through land-use management *Nat. Sustainabil.* **2** 122–9

Claverie M *et al* 2016 A 30+ Year AVHRR LAI and FAPAR climate data record: algorithm description and validation *Remote Sen.* **8** 263

Cook B I and Pau S 2013 Remote sensing a global assessment of long-term greening and browning trends in pasture lands using the GIMMS LAI3g dataset *Remote Sens.* **5** 2492–512

Cortés J *et al* 2021 Where are global vegetation greening and browning trends significant? *Geophys. Res. Lett.* **48** 6

de Jong R *et al* 2013 Shifts in global vegetation activity trends *Remote Sens.* **5** 1117–33

Dublin H T and Ogutu J O 2015 Population regulation of African buffalo in the Mara-Serengeti ecosystem *Wildlife Res.* **42** 382–93

Elsen P R *et al* 2020 Keeping pace with climate change in global terrestrial protected areas *Sci. Adv.* **6** 25

Estes A B *et al* 2012 Land-cover change and human population trends in the greater Serengeti ecosystem from 1984-2003 *Biol. Conserv.* **147** 255–63

Fang H *et al* 2013 Characterization and intercomparison of global moderate resolution leaf area index (LAI) products: analysis of climatologies and theoretical uncertainties *J. Geophys. Res.: Biogeosci.* **118** 529–48

Forkel M *et al* 2016 Enhanced seasonal CO_2 exchange caused by amplified plant productivity in northern ecosystems *Science* **351** 696–9

Funk C *et al* 2015 The climate hazards infrared precipitation with stations—a new environmental record for monitoring extremes *Sci. Data* **2** 150066

Goward and N S 1985 Analysis of terrestrial conditions and dynamics *Tech. Rep.*

Graham M H 2003 Confronting multicollinearity in ecological multiple regression *Ecology* **84** 2809–15

Green D S *et al* 2019 Long-term ecological changes influence herbivore diversity and abundance inside a protected area in the Mara-Serengeti ecosystem *Global Ecol. Conserv.* **20** e00697

Guo B *et al* 2016 Analysis of the nonlinear trends and non-stationary oscillations of regional precipitation in Xinjiang, northwestern China, using ensemble empirical mode decomposition *Int. J. Environ. Res. Public Health* **13** 345

Harris I *et al* 2020 Version 4 of the CRU TS monthly high-resolution gridded multivariate climate dataset *Sci. Data* **7** 1–18

Hawinkel P *et al* 2016 Vegetation response to precipitation variability in East Africa controlled by biogeographical factors *J. Geophys. Res.: Biogeosci.* **121** 2422–44

Huang N E *et al* 1998 The empirical mode decomposition and the hilbert spectrum for nonlinear and non-stationary time series analysis *Proc. R. Soc.* A **454** 903–95

Hunninck L *et al* 2020 Consequences of climate-induced vegetation changes exceed those of human disturbance for wild impala in the Serengeti ecosystem *Conserv. Physiol.* **8** 1

Jones K R *et al* 2018 One-third of global protected land is under intense human pressure *Science* **360** 788–91

Kalisa W *et al* 2019 Assessment of climate impact on vegetation dynamics over East Africa from 1982 to 2015 *Sci. Rep.* **9** 1–20

Kendall M G 1948 *Rank Correlation Methods* (London: Charles Griffin & Co. Ltd.) p 160

Kija H K *et al* 2020 Spatio-temporal changes in wildlife habitat quality in the greater Serengeti ecosystem *Sustainability* **12** 1–19

Kilungu H *et al* 2017 Climate change threatens major tourist attractions and tourism in Serengeti National Park, Tanzania *Climate Change Adaptation in Africa* (Cham: Springer) pp 375–92

Landmann T and Dubovyk O 2014 Spatial analysis of human-induced vegetation productivity decline over eastern Africa using a decade (2001-2011) of medium resolution MODIS time-series data *Int. J. Appl. Earth Obs. Geoinf.* **33** 76–82

Li W *et al* 2020 Accelerating savanna degradation threatens the Maasai Mara socio-ecological system *Glob. Environ. Change* **60**

Li X *et al* 2017 A new global land-use and land-cover change product at a 1-km resolution for 2010 to 2100 based on human-environment interactions *Ann. Am. Assoc. Geogr.* **107** 1040–59

Liang S *et al* 2013 A long-term global land surface satellite (GLASS) data-set for environmental studies *Int. J. Digital Earth* **6** 5–33

Liu X *et al* 2020 Characteristics of temperature evolution from 1960 to 2015 in the three rivers' headstream region, Qinghai, China *Sci. Rep.* **10** 1–17

Liu Y *et al* 2015 Spatial and temporal patterns of global NDVI trends: correlations with climate and human factors *Remote Sens.* **7** 13233–50

Martens B *et al* 2017 GLEAM v3: satellite-based land evaporation and root-zone soil moisture *Geosci. Model Dev.* **10** 1903–25

Masselot P *et al* 2018 EMD-regression for modelling multi-scale relationships and application to weather-related cardiovascular mortality *Sci. Total Environ.* **612** 1018–29

Midgley G F and Bond W J 2015 Future of African terrestrial biodiversity and ecosystems under anthropogenic climate change *Nat. Clim. Chang.* **5** 9

Mondal P, McDermid S S and Qadir A 2020 A reporting framework for sustainable development goal 15: multi-scale monitoring of forest degradation using MODIS, landsat and sentinel data *Remote Sens. Environ.* **237** 111592

Myneni R *et al* 2015 *MCD15A3H MODIS/Terra+Aqua Leaf Area Index/FPAR 4-day L4 Global 500m SIN Grid V006* (https://doi.org/10.5067/MODIS/MCD15A3H.006)

Nemani R R *et al* 2003 Climate-driven increases in global terrestrial net primary production from 1982 to 1999 *Science* **300** 1560–3

Nicholson S E 2015 The predictability of rainfall over the Greater Horn of Africa. Part II: prediction of monthly rainfall during the long rains *J. Hydrometeorol.* **16** 2001–12

Nicholson S E 2017 Climate and climatic variability of rainfall over eastern Africa *Rev. Geophys.* **55** 590–635

Nkwabi A K *et al* 2019 Bird community responses to changes in vegetation caused by increasing large mammal populations in the Serengeti woodlands *Wildlife Res.* **46** 256–64

Ogutu J O *et al* 2008 El Niño-Southern Oscillation, rainfall, temperature and normalized difference vegetation index fluctuations in the Mara-Serengeti ecosystem *African J. Ecol.* **46** 132–43

Pan N et al 2018 Increasing global vegetation browning hidden in overall vegetation greening: insights from time-varying trends *Remote Sens. Environ.* **214** 59–72
Pelkey S C and Caro T 2003 Assessing habitat protection regimes in tanzania using AVHRR NDVI composites: comparisons at different spatial and temporal scales *Int. J. Remote Sens.* **24** 2533–58
Pettorelli N et al 2012 Tracking the effect of climate change on ecosystem functioning using protected areas: Africa as a case study *Ecol. Indicators* **20** 269–76
Probert J R et al 2019 Anthropogenic modifications to fire regimes in the wider Serengeti-Mara ecosystem *Global Change Biol.* **25** 3406–23
Rannow S et al 2014 Managing protected areas under climate change: challenges and priorities *Environ. Manage.* **54** 732–43
Ritchie M E 2008 Global environmental changes and their Impact on the Serengeti *Serengeti III: Human Impacts ON Ecosystem Dynamics* 1st edn, ed A R E Sinclair, C Packer, S A R Mduma and J M Fryxel (Chicago: University of Chicago Press) ch 6, p 512
Ryan C M et al 2017 Pre-rain green-up is ubiquitous across southern tropical Africa: implications for temporal niche separation and model representation *New Phytol.* **213** 625–33
Sang Y F, Wang Z and Liu C 2014 Comparison of the MK test and EMD method for trend identification in hydrological time series *J. Hydrol.* **510** 293–8
Scheffers B et al 2016 The broad footprint of climate change from genes to biomes to people *Science* **354**
Schreiber T and Schmitz A 1996 Improved surrogate data for nonlinearity tests *Phys. Rev. Lett.* **77** 635–8
Sinclair A R et al 2014 Responses of the Serengeti avifauna to long-term change in the environment *Ostrich* **85** 1–11
Sinclair A R et al 2008 Historical and future changes to the serengeti ecosystem *Serengeti III: Human Impacts ON Ecosystem Dynamics* 1st edn, ed A R E Sinclair, C Packer, S A R Mduma and J M Fryxel (Chicago: University of Chicago Press) ch 2, p 512
Stolton S, Shadie P and Dudley N 2013 *Iucn Wcpa Guidelines for Applying Protected Area Management Categories* 21st edn (Gland, Switzerland: IUCN)
Theiler J et al 1992 Testing for nonlinearity in time series: the method of surrogate data *Physica* D **58** 77–94
Ugbaje S U and Bishop T F 2020 Hydrological control of vegetation greenness dynamics in Africa: a multivariate analysis using satellite observed soil moisture, terrestrial water storage and precipitation *Land* **9** 15
UN General Assembly 2015 Transforming our world: the 2030 Agenda for Sustainable Development A/RES/70/1
Veldhuis M P et al 2019 Cross-boundary human impacts compromise the Serengeti-Mara ecosystem *Science* **363** 1424–8
Venter O, et al 2016 Sixteen years of change in the global terrestrial human footprint and implications for biodiversity conservation *Nat. Commun.* **7** 12558
Walker A P et al 2020 Integrating the evidence for a terrestrial carbon sink caused by increasing atmospheric CO_2 *New Phytol.* **229** 5
Wei F et al 2018 Vegetation dynamic trends and the main drivers detected using the ensemble empirical mode decomposition method in East Africa *Land Degrad. Dev.* **29** 2542–53
Williams A P and Funk C 2011 A westward extension of the warm pool leads to a westward extension of the Walker circulation, drying eastern Africa *Clim. Dyn.* **37** 2417–35
Wu Z and Huang N E 2009 Ensemble empirical mode decomposition: a noise-assisted data analysis method *Adv. Data Sci. Adapt. Anal.* **1** 1–41
Xiao Z, Liang S and Jiang B 2017 Evaluation of four long time-series global leaf area index products *Agri. Forest Meteorol.* **246** 218–30
Yang A C et al 2011 Temporal associations between weather and headache: analysis by empirical mode decomposition *PLoS One* **6** 1–6
Yuan H et al 2011 Reprocessing the MODIS Leaf Area Index products for land surface and climate modelling *Remote Sens. Environ.* **115** 1171–87
Zhang X et al 2005 Monitoring the response of vegetation phenology to precipitation in Africa by coupling MODIS and TRMM instruments *J. Geophys. Res.: Atmos.* **110** D12
Zhang X, Friedl M A and Schaaf C B 2006 Global vegetation phenology from moderate resolution imaging spectroradiometer (MODIS): evaluation of global patterns and comparison with in situ measurements *J. Geophys. Res.: Biogeosci.* **111**
Zhu Z et al 2013 Global data sets of vegetation leaf area index (LAI)3g and fraction of photosynthetically active radiation (FPAR)3g derived from global inventory modeling and mapping studies (GIMMS) normalized difference vegetation index (NDVI3G) for the period 1981 to 2 *Remote Sens.* **5** 927–48
Zhu Z et al 2016 Greening of the Earth and its drivers *Nat. Clim. Change* **6** 791–5